

# UC Berkeley

## UC Berkeley Previously Published Works

### Title

Microbial Sulfate Reduction and Perchlorate Inhibition in a Novel Mesoscale Tank Experiment

### Permalink

<https://escholarship.org/uc/item/8sm5094r>

### Journal

Energy & Fuels, 32(12)

### ISSN

0887-0624

### Authors

Cheng, Yiwei  
Wu, Yuxin  
Wen, Hang  
[et al.](#)

### Publication Date

2018-12-20

### DOI

10.1021/acs.energyfuels.8b01802

Peer reviewed

# Microbial Sulfate Reduction and Perchlorate Inhibition in a Novel Mesoscale Tank Experiment

Yiwei Cheng,<sup>†</sup> Yuxin Wu,<sup>\*,†</sup> Hang Wen,<sup>‡</sup> Christopher G. Hubbard,<sup>†,#</sup> Anna L Engelbrekton,<sup>§,||</sup> Lauren Tom,<sup>†</sup> Li Li,<sup>‡</sup> Yvette Piceno,<sup>†,∇</sup> Markus Bill,<sup>†</sup> Gary Andersen,<sup>⊥</sup> John D. Coates,<sup>§,||</sup> Mark E. Conrad,<sup>†</sup> and Jonathan B. Ajo-Franklin<sup>†</sup>

<sup>†</sup> Earth and Environmental Sciences Area and <sup>⊥</sup>BioSciences Area, Lawrence Berkeley National Laboratory, Berkeley, California, United States <sup>‡</sup> Department of Civil and Environmental Engineering, Pennsylvania State University, University Park, Pennsylvania, United States <sup>§</sup> Energy Biosciences Institute and <sup>||</sup> Department of Plant and Microbial Biology, University of California, Berkeley, California, United States

## Abstract

Microbial sulfate reduction occurs ubiquitously in natural environments. In oil and gas reservoirs, the generation of sulfide (also known as souring) can result in the corrosion of steel infrastructure and downgrading of oil quality, among other environmental and health-related concerns. The complex interplay between hydrological, geochemical, and biological processes during souring is poorly understood, preventing effective treatment and mitigation especially in naturally heterogeneous subsurfaces. In this work, three-dimensional flow tank experiments are utilized as a mesoscale experiment that links well-constrained batch and column experiments to field measurements. The mesoscale tank experiment investigating perchlorate treatment of souring is coupled with reactive transport modeling to understand the effects of heterogeneity on souring and effectiveness of perchlorate treatment. Tracer experiments were conducted at the start and end of the experiment to constrain flow pathways and heterogeneities. Isotopic, geochemical, and microbial data revealed that perchlorate effectively inhibited sulfidogenesis and the growth of dominant sulfate reducing *Desulfobacteraceae*. Perchlorate treatment enriched *Desulfobulbaceae*, a sulfur-oxidizing group of bacteria, and *Sulfurimonas*, a potential perchlorate reducer. More organisms, including sulfate reducing bacteria, were observed closer to the influent. Results from the three-dimensional reactive transport model indicate horizontal preferential flows, as a result of the permeability contrast, led to faster bacteria growth (sulfate reducing bacteria) and sulfate reduction in fast flow regions. This work highlights the control that spatial distributions of hydrologic characteristics exert over reservoir souring and treatment.

## 1. Introduction

Sulfate reduction plays an important role in the global sulfur cycle. In the context of oil production, sulfate reduction occurs during secondary oil production, where seawater, rich in sulfate in comparison to typical subsurface brines, is injected into oil reservoirs to maintain reservoir pressure and increase sweep efficiency. The hydrogen sulfide ( $H_2S$ ) produced by sulfate reduction (also known as microbial souring) leads to corrosion and facility degradation, health and safety hazards, among other concerns. (1–4) The efficacy of any desouring treatment is complicated by the interplay between hydrological, geochemical, and biological processes in the subsurface. Understanding and preventing oil reservoir souring remain an ongoing challenge for oil and gas production, particularly for off-shore fields under pressure management.

Experiments conducted to elucidate primary controls over souring or sweetening (desouring), the removal of  $H_2S$  and organosulfide compounds, typically fall into one of the two ends of the complexity spectrum. On one end are the well-constrained, homogeneous systems represented by microcosms and flow-through bioreactors. Microcosm experiments conducted using serum bottles are closed systems with well-characterized media (e.g., synthetic growth media or reservoir fluid samples from produced wells) that are amenable to tracking of mass balances (e.g., chemical species), characterization of growth of sulfate reducing microorganisms (SRM), and investigation of dosage of inhibitors (e.g., nitrate, perchlorate) for effective souring treatment.(5–8) Additional complexities are introduced in flow-through bioreactors or columns. Microbial communities are no longer growing in suspension but in matrices of the materials packed into the columns: a more realistic environment, particularly for biofilm development. While flow is introduced (normally from bottom to top) to simulate the injection well environment, it represents a simple one-dimensional (1D) flow regime macroscopically. Therefore, with known flow rates, chemical makeup of the influent and effluent fluids, system mass balances are still tractable. Column studies have investigated the impacts of nitrate/nitrite amendment on sulfide production with different electron donors (e.g., lactate, volatile fatty acids (VFAs), crude oil).(5,9–11) Recently, Engelbrektsen et al.(12) and Wu et al.(13) compared the effectiveness of different inhibitors (i.e., nitrate and (per)chlorate) on biogenic sulfide production, and in subsequent follow-up column studies, the impact of different inhibitor dosages.(14) On the other end of the spatial/process complexity spectrum are experimental studies conducted in situ. Most field studies targeting souring at depth are highly under-constrained and have poorly defined boundary conditions and limited sampling and information on the spatial heterogeneity of biogeochemical parameters. Field studies were conducted to study the effectiveness of nitrate as a souring treatment under various reservoir-operating conditions.(15–19) To our knowledge, no field trials of (per)chlorate treatment currently exist.

It is generally acknowledged that the complexities of deep subsurface environments are difficult to capture in laboratory studies. Microbial communities in reservoir formations form biofilms within fractures in oil bearing rock formations and mineral matrices,(20) with the partitioning between biofilm phase and planktonic phase typically not well-known. This is in contrast to the planktonic conditions of microbial cells grown in suspension in the microcosm studies. While environmental conditions in laboratory scale experiments are held constant, they are variable in the field; the rates and chemical makeup of the injection brines for waterfloods often vary depending on the ratio of produced water included, and fields often have shut-in periods associated with equipment maintenance. The electron donor pool used by subsurface organisms is also often unknown due to the abundance of hydrocarbons available and their unknown spatial distribution. Lastly, the scale mismatch between laboratory (mm-m) and field (km) lengths also lead to mismatch in flow transit and residence times.(20)

Another key control over reactive transport processes not typically captured in simple laboratory experiments is spatial heterogeneity in both physical and geochemical properties. Studies in other natural subsurface systems have revealed the role spatial heterogeneity plays in controlling flow and solute transport, and determining how and to what extent biogeochemical reactions occur.(21–27) Li et al.(23) demonstrated that spatial distribution of hydraulic conductivity and iron oxides control the flow and the contact time between organic carbon, iron oxides, and microbe, and ultimately field-scale bioreduction rates. In reservoir souring, spatial variations in hydrologic properties such as porosity and hydraulic conductivity can potentially impact the distribution of injected seawater/produced water within the reservoir. In natural systems with multiple flow layers, the organics and souring microbiota have to reside in the flow paths of sulfate (electron acceptor in seawater/produced water). Despite the importance of heterogeneities, characterization of field sites at adequate resolutions is often challenging both logistically and economically. As such, limitations exist in the translation of results from laboratory experiments to natural systems, where heterogeneity is ubiquitous.

Numerical models are useful tools in exploring questions related to oil reservoir souring. Process-based models differentiate the key governing processes and provide systematic views that integrate disparate processes and data sets.(13,28–32) A multiphase/component general-purpose adaptive reservoir simulator (GPAS) was developed to simulate souring and nitrate treatment at both the column and field scales.(29) Reactive transport models of perchlorate treatment were developed with data from column experiments to gain insight into the underlying competing mechanisms controlling the action of perchlorate.(13,31) In all, most modeling studies on souring and perchlorate treatment to date focused on the representation of biogeochemical processes in systems with relatively simple flow and transport.

The influence of heterogeneous flow paths on the microbial growth and biogeochemical reactions are not well captured in existing column experiments and are poorly constrained in field studies. In this study, a novel three-dimensional (3D) mesoscale tank experiment was designed with the goal of elucidating the heterogeneous spatiotemporal evolution of chemical species and microbial populations in the mesoscale system. Perchlorate was introduced after the system had been allowed to sour to determine where (or when), and to what extent, sweetening (desouring) could be achieved with respect to flow path and which bacteria were involved in sulfur cycling in this mesoscale system. The comprehensive data set generated from the experiment was utilized in the development and validation of a 3D reactive transport model. The model captured the spatiotemporal trends of the chemical species and microbial populations that emerged as a result of feedbacks between microbes, flow, and the minerals. In addition, simulations revealed the important role of flow field heterogeneity in controlling system scale sulfate reduction rates.

## 2. Methods

### 2.1. Experimental Set-up and Operation

A 20" (50.8 cm) by 12" (30.5 cm) by 12" (30.5 cm) ( $L \times W \times H$ ) tank was constructed using polycarbonate. The bottom of the tank was first packed with a 5" (12.7 cm) thick sand (Ottawa, 20/20 mesh, 0.6–0.85 mm in diameter) overlaid by a 2" (5.1 cm) thick bentonite clay layer, and then a 4" (10.2 cm) thick sand (Ottawa) layer on top. The final result was a three-layer model with a confined formation as the target formation at the bottom (Figure 1).

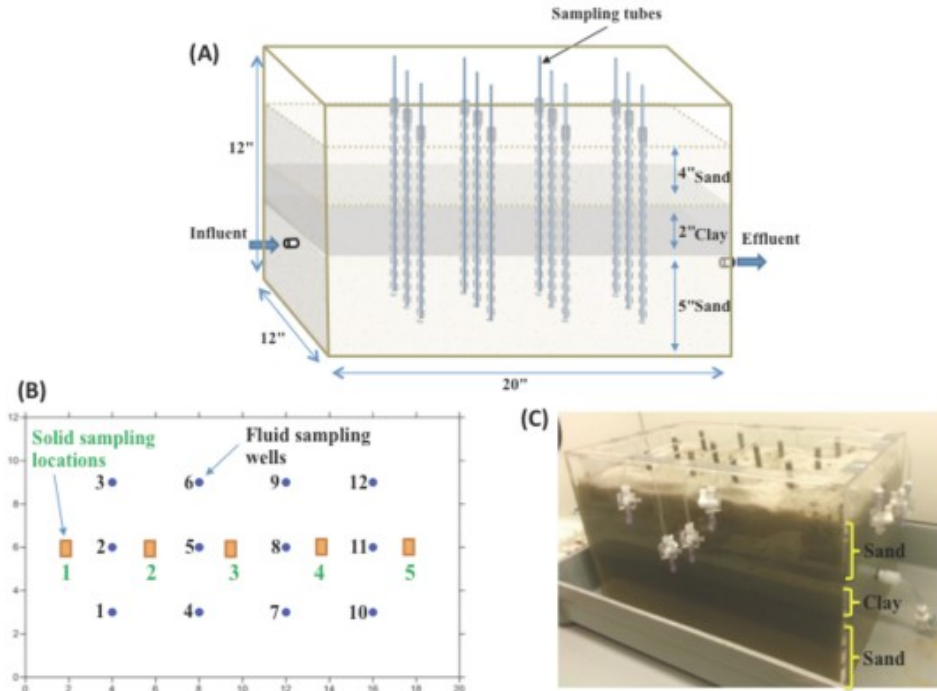


**Figure 1.** (A) Setup for the mesoscale biosouring and desouring experiment. A three-layer model was built for this experiment with a confined layer at the bottom of the tank as the target formation. Twelve low carbon steel electrodes were installed to simulate wellbores, and sampling tubes were imbedded in the steel tubes for fluid sampling. (B) Schematic aerial view of the tank showing fluid and solid sampling locations. (C) Photograph of the tank.

Due to their large quantities, the sand and clay packed into the tank were not sterilized. Twelve low-carbon steel hollow tubes (1/4" OD and 1/8" ID) with embedded plastic tubing were installed in the tank as pore water sampling wells and to simulate the near borehole conditions in terms of iron corrosion and chemistry (Figure 1). The sampling tubes were positioned ~1 cm from the bottom of the tank within the confined layer. Fiberglass wool was inserted into the bottom of the embedded plastic tubing for filtration. Autoclaved bay water from the San Francisco Bay (sulfate concentration:  $26.8 \pm 1.3$  mM, mean  $\pm 1\sigma$ ,  $n = 26$ ) was used as the saturating media as well as the carrier fluid for nutrients and treatments throughout the experiments. The selection of bay water was made to simulate secondary recovery with seawater flooding and to evaluate the effects of high salinity and complex water chemistry on the souring process and the effectiveness of the perchlorate treatments. 10 mM acetate was added to the bay water as the carbon source, initiating souring, and subsequently 10 mM perchlorate was added during the treatment period. The second period started once significant amounts of sulfide were measured in the sampling wells and the effluents. All solutions were autoclaved at ~120 °C for 1 h and kept under nitrogen headspace (1–2 psi) throughout the experiments to maintain an anaerobic environment similar to the conditions in the oil reservoirs. The flow rates were regulated with peristaltic pumps and maintained at  $\sim 0.4$  mL min<sup>-1</sup> throughout the experiments.

The experiment can be divided into a few key stages. The tank was first flooded with seawater to establish steady-state flow conditions (Phase A), followed by the first tracer test with fluorescein on Day -28 (Phase Ai, Day 0 being the start of the souring phase). The tank was inoculated with SRM-containing microbial community (enriched from San Francisco bay mud with acetate as electron donor) on Day -16 (Phase B). After inoculation, the flow was paused for 6 days to allow the microbial community to establish. Flow was resumed and the souring phase began on Day 0 (Phase C). On Day 65 (Phase D), the sweetening phase began with the addition of 10 mM perchlorate to the influent solution. After a shut-in period (Phase E), flow was resumed (F) and a final tracer test with bromide was conducted on Day 153 (Phase Fi). The experiment concluded on Day 182. Details on the timing and the different phases of the experiment are outlined in Table 1.

**Table 1. Different Phases of the Experiment**

day	phase	description
	A	Initial saturation of the tank with seawater. Baseline flow conditions established.
-28	Ai	initial tracer test with fluorescein
-16	B	inoculation followed by shut-in
0	C	sulfidogenesis phase
65	D	addition of 10 mM perchlorate
99	E	shut-in
124	F	flow restarted
153	Fi	bromide tracer test started
182		end of flow
196		solid samples excavated from tank

Two separate tracer tests were conducted over the course of the experiment to elucidate the hydrological characteristics of the tank system: (1) A fluorescent dye tracer study (Phase Ai) — before the tank system was inoculated with microbial community, (2) A bromide tracer study — before the conclusion of the experiment. The fluorescent dye tracer test was administered for 3.5 h at 0.87 mL/min and an injection concentration of 10 ppm. In the bromide tracer study, bromide concentration in the influent was raised from a baseline concentration of 0.83–6.53 mM on Day 153 and returned to the baseline level on Day 167.

## 2.2. Sampling and Analysis

Liquid was sampled from the 12 sampling wells throughout the experiment. Approximately 5–8 mL was extracted and filtered (0.2  $\mu$ m) for sulfide measurements and anion, dissolved iron (acidified to 0.1 M HCl), and sulfur isotope analysis. One milliliter unfiltered samples for microbial analyses were stored at -80 °C for five different sampling points throughout the experiment: Initial (Day 0), after souring (Day 65), after perchlorate treatment (Day 89), after the shut-in period (Day 124), and upon cessation of the experiment (Day 182). Influent samples were also collected at the start and end of each replenish of the influent.

Dissolved sulfide concentrations were determined immediately after sampling using colorimetric techniques.(33,34) Anion concentrations (sulfate, chloride, perchlorate, acetate, and bromide) were determined by ion chromatography (Dionex), while total dissolved iron was analyzed colorimetrically.(35) Sulfur isotope ratios of dissolved sulfate samples from each treatment were reported in standard delta notation relative to the Canyon Diablo Troilite standard ( $R_{std} = 0.0441216$ ) as  $\delta^{34}\text{S}$  (‰) =  $(R_{sample}/R_{std} - 1) \times 1000$ , where  $R = {}^{34}\text{S}/{}^{32}\text{S}$ , and the value is reported in per mil units (‰). Details of sulfur isotope analysis can be found in the Supporting Information.

Solid phase samples were excavated from the tank at the end of the experiment. Samples were taken from both the middle of the top layer of sand and from close to the bottom of the tank. Subsamples were stored at  $-80\text{ }^{\circ}\text{C}$  for microbial analysis. Subsamples were also air-dried and digested in HCl to release bioavailable iron (0.5 M HCl digest on a shaker for 30 min) or total iron (6 M HCl digest on a shaker for 8 h).(36) The digests were analyzed for iron by ICP-MS (PerkinElmer).

The sediment and water samples were analyzed for both microbial community composition using the iTag procedure (see SI for details) and total counts using quantitative PCR (qPCR). qPCR targeting the total 16S rRNA and the *dsrA* genes was carried out using three different primer sets: Bourne, Kondo, and Chin (see Supporting Information for details); two *dsrA* gene primer sets were used to provide greater coverage of known SRM than either set alone. For community composition, genomic DNA was extracted from either sediment (0.5 g) or water samples (950uL pelleted via centrifugation) using a PowerSoil DNA Isolation Kit (MoBio, Carlsbad, CA). iTag PCR was carried out using primers 515F and barcoded 806R. (37,38) Further method details for sample preparation and data analysis are available in the Supporting Information.

### 2.3. Reactive Transport Modeling

CrunchTope,(39) a reactive transport code, was used to develop a mechanistic model of the coupled biochemical and flow processes that occurred in the tank. In CrunchTope, dynamics relating bacterial growth and energetics follow the conceptual framework as described in Rittmann et al. (40) In the environment, microorganisms (MB) mediate the reaction between an electron donor and an electron acceptor (i.e., sulfate and perchlorate in this study) to derive energy for growth and maintenance. Rates of microbially mediated reactions are described as follows:

$$R = \mu[\text{MB}]K_T(1)$$

where  $R$  ( $\text{mol}/\text{m}^3$  porous media/s) represents the reaction rate as mediated by MB (represented as  $\text{C}_5\text{H}_7\text{O}_2\text{N}$ ), and  $\mu$  ( $\text{mol}/\text{mol}_{\text{C}_5\text{H}_7\text{O}_2\text{N}}/\text{s}$ ) is the maximum specific utilization rate. Kinetic constraints  $K_T$  on the reaction rate by electron



acceptors/donors and inhibitors are mathematically represented as

$$K_T = \frac{[eDonor]}{[eDonor] + K_{eDonor}} \frac{[eAcceptor]}{[eAcceptor] + K_{eAcceptor}} \frac{K_{Inhibitor}}{[Inhibitor] + K_{Inhibitor}} \quad (2)$$

$K_{eDonor/eAcceptor}$  (mol/L) is the half saturation (affinity constant) of the electron donor/acceptor, while  $K_{inhibitor}$  (mol/L) is the inhibition constant. The microbes in this model are assumed to be immobile as generally observed in subsurface systems, where most of the cells tend to attach onto the solid phase in the form of biofilms or separate microbial colonies.(40,41) Such understanding is also applicable in oil reservoirs: microbial communities in reservoir formations form biofilms within fractures in oil bearing rock formations and mineral matrices,(20) with the partitioning between biofilm phase and planktonic phase typically not well-known.

Rates of mineral dissolution and precipitation are calculated based on a rate law derived from transition state theory (TST).(42)

$$R = kA \left( 1 - \frac{IAP}{K_{eq}} \right) \quad (3)$$

where  $k$  is the reaction rate constant (mol/m<sup>2</sup>/s), IAP is the ion activity product,  $K_{eq}$  is the equilibrium constant of the reaction, and  $A$  is the reactive surface area of the mineral (m<sup>2</sup> surface area/m<sup>3</sup> porous media). Microbe-mediated and mineral reactions, and relevant parameters are listed in Tables 2–3.

**Table 2. Microbial and Iron-Sulfide Reactions Modeled<sup>a</sup>**

Microbial Reactions	
1	sulfate reduction ( $f_s = 0.08$ , $f_e = 0.92$ ) $0.115SO_4^{2-} + 0.125CH_3COO^- + 0.004NH_3(aq) + 0.23H_2O + 0.01H^+ \rightarrow$ $0.004C_3H_7O_2N_{SRB} + 0.23HCO_3^- + 0.115HS^-$
2	iron reduction ( $f_s = 0.40$ , $f_e = 0.60$ ) $FeOOH(s) + 0.208CH_3COO^- + 0.033NH_3(aq) + 1.925H^+ \rightarrow$ $0.033C_3H_7O_2N_{FeRB} + 0.25HCO_3^- + 1.6H_2O + Fe^{2+}$
3	heterotrophic perchlorate reduction ( $f_s = 0.20$ , $f_e = 0.80$ ) $0.125ClO_4^- + 0.15625CH_3COO^- + 0.0125NH_3(aq) \rightarrow$ $0.0125C_3H_7O_2N_{PRB} + 0.250HCO_3^- + 0.125Cl^- + 0.09375H^+ +$ $0.0375H_2O$
4	perchlorate reduction sulfide oxidation ( $f_s = 0.0$ , $f_e = 1.0$ ) $0.125ClO_4^- + 0.5H^+ + 0.5HS^- \rightarrow 0.125Cl^- + 0.5H_2O + 0.5S(aq)$
Iron-Sulfide Reactions	
5	$Fe^{2+} + H_2S(aq) \leftrightarrow FeS(am) + 2H^+$
6	$Fe(OH)_3(s) + 0.5H_2S(aq) \leftrightarrow Fe^{2+} + 0.5S(s) + H_2O + 2.0OH^-$

<sup>a</sup>Following the concepts as described by Rittmann and McCarty (2001), microbially mediated reactions are divided into two components: catabolic and anabolic. For each mole of electron donor/substrate utilized, a fraction,  $f_s$  is conserved by the microbial biomass for cell synthesis (anabolic) while the remaining fraction,  $f_e$  is used for energy production (catabolic). Values of  $f_s$  and  $f_e$  are determined by the types of electron donors and acceptors involved in the reaction using free energy values as described in Rittmann and McCarty.<sup>40</sup> The electron donor, electron acceptor and cell synthesis half equations are combined into a macrochemical stoichiometric equation (Reactions 1–4 below). Detailed description can be found in Supporting Information.

**Table 3. Physical and Chemical Parameters**

reaction no.	$\mu$ (mol/mol $\text{C}_5\text{H}_7\text{O}_2\text{N/s}$ )	$K_{a, \text{Acceptor}}$ (mol/L)	$K_{a, \text{Donor}}$ (mol/L)	$K_{i, \text{Inhibitor}}$ (mol/L)
1	$1.10 \times 10^{-3a}$	$1.25 \times 10^{-3b}$	$1.25 \times 10^{-3c}$	$1.90 \times 10^{-3d}$
2	$9.96 \times 10^{-5e}$	$235.0 \mu\text{mol/g}^f$	$1.00 \times 10^{-4g}$	
3	$3.17 \times 10^{-3}$	$1.25 \times 10^{-3}$	$1.25 \times 10^{-2}$	$3.25 \times 10^{-3h}$
4	$2.22 \times 10^{-4}$	$5.00 \times 10^{-4}$	$1.25 \times 10^{-3}$	
reaction no.	Log $k$		Log $K_{eq}$	
5	$-10.0^i$		$3.50^j$	
6	$-3.30^l$		$-19.60^l$	
Physical parameters				
porosity <sup>k</sup>			0.40	
dispersivity (cm) <sup>l</sup>			0.20 (longitudinal), 0.01 (transverse)	
molecular diffusion coefficient (m <sup>2</sup> /s) <sup>m</sup>			$6.00 \times 10^{-10}$	
cementation factor <sup>n</sup>			1.50	

<sup>a</sup>Range between  $1.13 \times 10^{-4}$  and  $1.20 \times 10^{-3}$  mol/mol  $\text{C}_5\text{H}_7\text{O}_2\text{N/s}$  based on Carlson et al.<sup>6</sup> <sup>b</sup>Range between  $1.00 \times 10^{-5}$  and  $7.50 \times 10^{-3}$  mol/L.<sup>50,51</sup> <sup>c</sup>Range between  $4.30 \times 10^{-6}$  and  $5.00 \times 10^{-3}$  mol/L.<sup>52</sup> <sup>d</sup>Perchlorate, range between  $2.00 \times 10^{-3}$  and  $3.00 \times 10^{-2}$  mol/L.<sup>6</sup> <sup>e</sup>The reaction rate of iron-reducing reaction is 2–30 times lower compared to Reaction (1), (3), and (4), probably due to the inherent properties of bacteria, different preferential carbon sources, and optimal growth temperature.<sup>53,54</sup> For example, the growth rate of iron-reducing bacteria can be over 10 times lower than sulfate-reducing bacteria under abundant nutrient conditions.<sup>55,56</sup> <sup>f</sup>Refs 57–59. <sup>g</sup>Refs 60 and 61. <sup>h</sup>Ref 31. <sup>i</sup>Refs 60 and 62. <sup>j</sup>Ref 63. <sup>k</sup>From experimental measurement. <sup>l</sup>Both dispersivities are calibrated from the experiment of nonreactive bromide transport, and within the range report in Gelhar et al.<sup>64</sup> <sup>m</sup>Molecular diffusion coefficient is set at a median value of  $6.0 \times 10^{-10}$  m<sup>2</sup>/s for among the diffusion coefficient of all species,<sup>65</sup> although the diffusion coefficients for individual aqueous species vary. This has negligible impact on simulated geochemical dynamics as transport is dominated by advection. <sup>n</sup>Ref 66.

## 2.4. Model Setup and Simulations

A three-dimensional flow and transport model of the confined bottom sand layer (within the tank, Figure 1) was set up in CrunchTope. The computational domain consisted of three horizontal planes (each with  $25.0 \times 16.0$  grids, resolution =  $2.0 \times 2.0$  cm) with thicknesses of 10.0 (10 grids at 1 cm resolution), 0.5 (1 grid at 0.5 cm resolution, where inlet and outlet points exist), and 2.0 cm (1 grid at 2.0 cm resolution), respectively. Except the inlet and outlet points, no-flux conditions are imposed for all the boundaries. Because the tracer concentrations in the monitoring wells indicate the presence of physical heterogeneity in the tank, inverse modeling of the tracer data was conducted to derive the heterogeneous characteristics of the 3D tank domain. Estimation of the spatial variations in permeability was conducted through the coupling of CrunchTope with the parameter estimation code, PEST,(43) and the parameter list processor, PLPROC, (44) while all other parameters (including porosity) were assumed to be spatially uniform. The inverse model assumes a steady flow field and that the variance and correlation structure of the permeability field is known a priori. Considering the typical permeability range of Ottawa sand ( $10^{-10}$  to  $10^{-11}$  m<sup>2</sup>) and the tank size, we assumed a medium-heterogeneous tank with a variance of 0.2 and correlation length of 9 cm in the horizon direction, within the typical range reported in the lab-scale sand tank.(45,46) Spatial distribution of permeability was generated using a geostatistical approach conditioned to unknown values at a number of locations (pilot points). (47) The inverse modeling simulated the tracer experiments, each time with different estimates of the permeability distribution, until the permeability distribution reproduced the tracer data within the specified criteria. Details of the geostatistical approach are described in Supporting Information, while relevant physical parameters are listed in Table3.

CrunchTope was utilized to simulate the transport and biogeochemical processes that occurred in the tank during souring (Phase C) and subsequent perchlorate treatment (Phase D). The kinetics of key terminal electron accepting processes (TEAPs) such as iron reduction, sulfate reduction, and perchlorate reduction (Table 2) were modeled following eq 1. In particular, three known microbiological mechanisms by which perchlorate reduces sulfide production are represented in the model: (1) indirect inhibition of the SRM through competition with heterotrophic perchlorate reducing microorganisms (hPRM) for electron donors, (2) direct inhibition of SRM activities by perchlorate, (48,49) and (3) perchlorate reducing sulfide oxidizing (PRSO) activity of the PRM. (7,8,12) Mehta-Kolte (8) demonstrated that PRMs mediate both heterotrophic perchlorate reduction and PRSO (to elemental sulfur, Table 2). The PRSO pathway is preferred; however, no growth is observed. PRM grow during heterotrophic perchlorate reduction, a metabolism that is only sustainable in the absence of sulfide. In the model, the PRM population mediates both pathways, with a sulfide inhibition constant applied to heterotrophic perchlorate reduction (Table 2). Parameter values for microbial reactions (Table 3) (e.g., maximum specific utilization rate) were calibrated with experimental data based on the best-fit heterogeneous domain derived from the above inverse modeling. Calibrated parameter values are within known parameter range from earlier studies (referenced in Table 3). To tease out the effects of a heterogeneous permeability field, another scenario of a homogeneous permeability field of  $1.0 \times 10^{-10} \text{ m}^2$  ( $k_x = k_y = k_z$ ) is added. The geochemical reaction network and corresponding parameters are the same with the best-fit heterogeneous case. Initial and influent concentrations of chemical species can be found in Tables 4-5.

**Table 4. Initial and Inlet Fluid Composition in the Tank Modeling**

aqueous species	initial concentrations in the tank (mol/L, except for pH)	concentrations in the inflowing fluid (mol/L, except for pH) <sup>a</sup>
pH	6.80	8.60
SO <sub>4</sub> (VI)	$3.80 \times 10^{-2}$	$3.38 \times 10^{-2}$
NH <sub>3(aq)</sub>	$1.00 \times 10^{-3}$	$1.25 \times 10^{-2}$
acetate	0.00	$1.25 \times 10^{-2}$
Na(I)	1.30	1.63
Cl(-I)	0.70	0.65
ClO <sub>4</sub> (VII)	0.00	0.00 (Phase C); $1.25 \times 10^{-2}$ (Phase D)
CO <sub>2(aq)</sub>	$3.43 \times 10^{-3}$	$1.34 \times 10^{-5}$
Fe(II)	$6.70 \times 10^{-4}$	0.00

<sup>a</sup>To incorporate the effects of evaporation, simulated inlet concentrations are all 1.25 times higher than experimental data.

**Table 5. Initial Concentrations of Mineral Volume Fraction and Biomass in the Tank Model**

mineral	volume fraction (m <sup>3</sup> /m <sup>3</sup> )
quartz	0.6
Goethite	$8.0 \times 10^{-5}$
FeOOH	$3.0 \times 10^{-5}$
biomass	initial concentrations (mol_C <sub>3</sub> H <sub>7</sub> O <sub>2</sub> N/L)
C <sub>3</sub> H <sub>7</sub> O <sub>2</sub> N <sub>SRB</sub>	$2.5 \times 10^{-5}$
C <sub>3</sub> H <sub>7</sub> O <sub>2</sub> N <sub>FeRB</sub>	$2.5 \times 10^{-5}$
C <sub>3</sub> H <sub>7</sub> O <sub>2</sub> N <sub>PRB</sub>	$1.2 \times 10^{-5}$

### 3. Results

#### 3.1. Tracer Tests and Flow Characteristics

The initial fluorescent dye tracer test showed that breakthrough began at ~40 h after injection and peaked after another 20 h, followed by exponential decrease over a period of ~60 h. In all, 47% of the dye injected was recovered after ~4.5 days (until effluent concentrations were below detection limit), indicating rather strong dispersion of the dye tracer within the tank (Figure 2B). The incomplete dye recovery can also be attributed to adsorption (e.g., to the clay layer) and possible degradation. The final bromide tracer study revealed heterogeneity within the porous media. Spatial concentration of bromide changed with time as shown in Figure 2C. Bromide concentrations in Wells 1, 4, 7, and 10 of the tank were higher than concentrations in Wells 3, 6, 9 and 12, suggesting the presence of preferential flow paths in the system. Results of both tracer experiments were used to generate hydrological parameters for the flow component of the reactive transport model, i.e., 3D distribution of heterogeneous permeability.

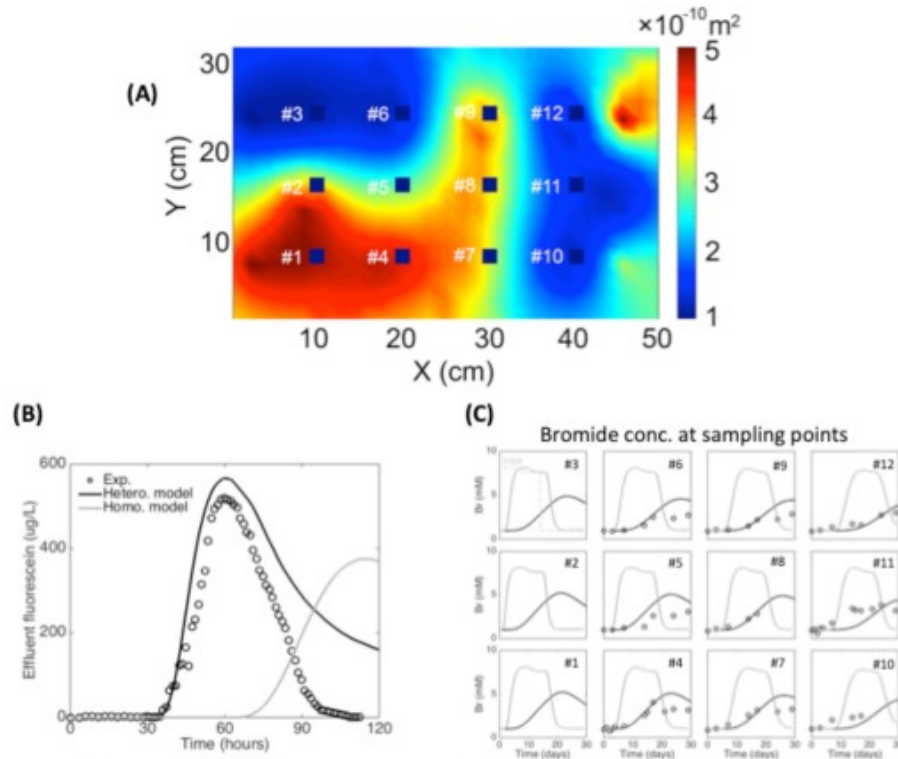


**Figure 2.** Permeability ( $k$ ) distribution and modeled tracer dynamics. (A) Image showing permeability ( $k$ ) distribution in a horizontal plane of the domain. 3D heterogeneous permeability ( $k$ ) distribution by inverse model PEST.  $k_x = k_y$  in the horizontal ( $XY$ ) direction and correlation length = 9.0 cm;  $k_z = 1.6 \times 10^{-11} \text{ m}^2$ ; same for all  $z$  layers. The 12 low-permeability square zones (dark blue) represent the wells and close-to-well areas. Considering the sand packing procedure, the close-to-well areas are assumed to have relatively low permeability with a value of  $10^{-11} \text{ m}^2$ . (B) Observed data (dots) and simulations (heterogeneous model: black line, homogeneous model: gray line) of fluorescein tracer test (conducted on Day 0 for the souring phase). (C) Observed data (dots) and simulations (heterogeneous model: black line, homogeneous model: gray line) of bromide tracer test.

Figure 2A shows a realization of the permeability ( $k$ ) distribution in a horizontal plane of the domain, derived through the inversion of the fluorescein and  $\text{Br}^-$  tracer data. In this permeability field,  $k_x = k_y$  in the horizontal ( $XY$ ) direction and correlation length = 9.0 cm. Values of  $k_z$  are the same for all layers in the vertical direction,  $k_z = 1.6 \times 10^{-11} \text{ m}^2$ , except the close-to-well regions with low  $k_x$ ,  $k_y$ , and  $k_z$ .

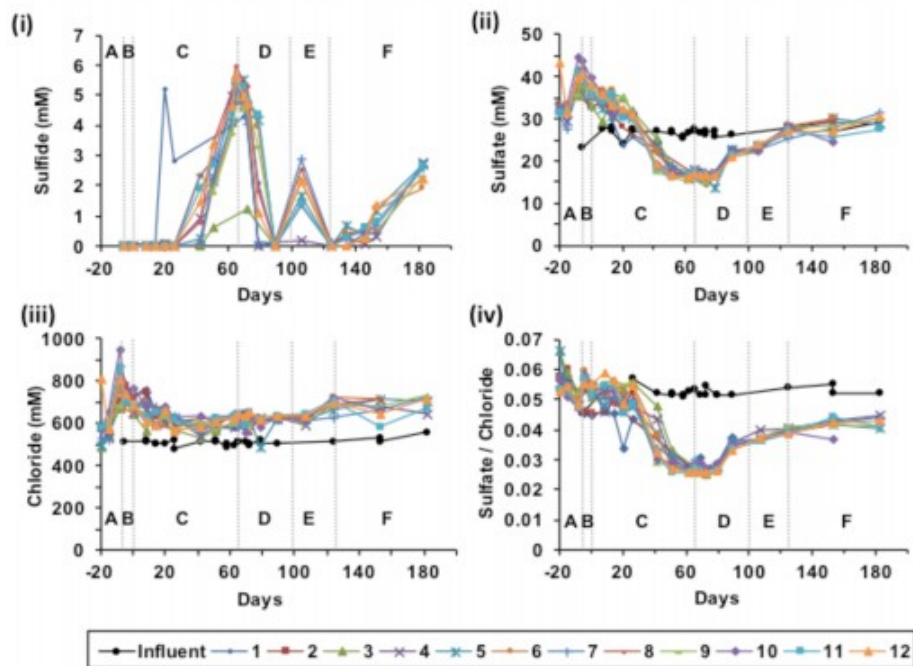
Figure 2B shows the comparison between simulations (both heterogeneous and homogeneous scenarios) and experimental data from the initial fluorescein tracer test. In the heterogeneous permeability field scenario (dark line), the simulated effluent fluorescein followed the observed fluorescein in timing and magnitude of the breakthrough curve. However, the simulated fluorescein breakthrough curve diverged from the observed fluorescein breakthrough curve in the recession phase. At  $\sim 110 \text{ h}$ , observed effluent fluorescein was at zero, while simulated effluent fluorescein was at  $\sim 150 \text{ } \mu\text{g/L}$ . In the homogeneous permeability field scenario (gray line), it can be noted that the simulated fluorescein breakthrough occurs much later,  $\sim 70 \text{ h}$ , almost double the amount of time for that of the heterogeneous case. In addition, to the delayed response time, the peak of the simulated curve was also much lower than the heterogeneous case, at  $\sim 400 \text{ } \mu\text{g/L}$ .

Figure 2C shows the comparison between modeled  $\text{Br}^-$  breakthrough curves and the observed  $\text{Br}^-$  breakthrough data at the 12 wells. In the heterogeneous permeability field scenario (dark line), it can be seen that modeled  $\text{Br}^-$  curves provide a good fit to the observed  $\text{Br}^-$  data. In addition to the tracer tests, chloride was present in the injection fluid throughout the experiment and acted as a conservative tracer during Phase C. Observed data showed a drop from initial concentration range of 700–780 mM to concentration range of 550–650 mM from ~ Day 15 to Day 30. Thereafter, the chloride concentration remained constant within the lower range (Figure S1, Supporting Information). In the simulation, the chloride concentration was set to 700 mM throughout the tank in the beginning. The chloride concentration in the injection fluid was 650 mM (Table 4). The simulated chloride concentration captured the initial drop in concentration, indicating that the model has adequately captured the flow dynamics of the system. In contrast to the heterogeneous scenario, it can be observed that the modeled  $\text{Br}^-$  for the homogeneous scenario (gray line) does not capture the flow dynamics as reflected by the experimental data. The simulated  $\text{Br}^-$  curves breakthrough much earlier and peaked at higher levels than the heterogeneous scenario.

## 3.2. Geochemical Species Concentrations

### 3.2.1. Temporal Variations From Sampling Wells

Figures 3 and 4 show the temporal variations in aqueous chemistry from different wells and the tank influent. Sulfide concentrations generally started to increase above 0.1 mM between 26 and 42 days into Phase C, after starting flow with 10 mM acetate. The earliest sulfide concentrations detected were in Well 1, rising from 0.04 mM on Day 8 to 5.2 mM on Day 20. Sulfide concentrations across the tank peaked at  $5.3 \pm 0.4$  mM ( $n = 9$ ) on Day 65, after which 10 mM perchlorate was added (Phase D) and dissolved sulfide was eliminated by Day 89. Sulfide concentrations showed a transitory high during shut-in (Phase E) but were not detected when flow was resumed (Phase F), climbing steadily at all sampled wells to  $2.0 \pm 0.9$  mM ( $n = 9$ ) by Day 182.



**Figure 3.** Dissolved sulfide (i), sulfate (ii), and chloride (iii) concentrations, and sulfate/chloride ratio (iv), in influent and well samples. Experimental phases correspond to Table 1 and are represented as letters bounded by vertical dashed lines. A = baseline saturation, B = inoculation, C = sulfidogenesis, D = perchlorate addition, E = shut-in, F = post shut-in.

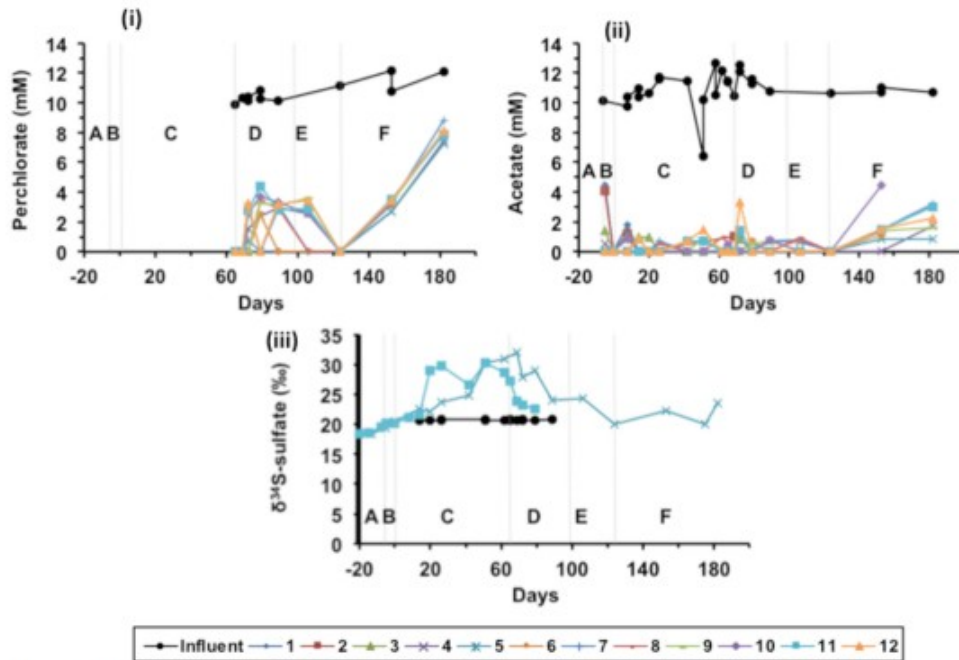


**Figure 4.** Dissolved perchlorate (i), acetate (ii), and  $\delta^{34}\text{S}$ -sulfate (iii), in influent and well samples. Experimental phases correspond to Table 1 and are represented as letters bounded by vertical dashed lines. A = baseline saturation, B = inoculation, C = sulfidogenesis, D = perchlorate addition, E = shut-in, F = post shut-in.

Sulfate concentrations measured in the wells during the early stages of the experiment were higher than the influent values (Figure 3B). A similar phenomenon was observed for chloride as well. Specifically, the chloride

concentration of the influent was consistent at  $513 \pm 15$  mM ( $n = 26$ ). However, chloride concentrations measured in the tank were both more variable and considerably higher than the influent ( $643 \pm 68$  mM,  $n = 222$ ; Figure 3C). The increased concentrations of these ions in the tank were likely due to evaporation process that can be caused by the imperfect sealing of the middle clay layer under the high airflow rates in the fume hood. On the basis of the chloride concentration offset, a net effect of  $\sim 20\%$  increase in ion concentrations was calculated and taken into account in the modeling which will be discussed later, because chloride can be considered conservative. Sulfate concentrations in the tank were  $35.5 \pm 2.2$  mM (mean  $\pm 1\sigma$ ,  $n = 12$ ) when flow was started at Day 0, decreasing below influent values ( $26.8 \pm 1.3$  mM,  $n = 26$ ) to sustained mean values of 16–17 mM between Days 51–79, coinciding with peak sulfide production. Sulfate then increased from the middle of Phase D (perchlorate addition) onward to reach values similar to influent concentrations during Phase F. The sulfate/chloride ratio provides a good indicator of sulfate reduction and is shown in Figure 3D, with values in the tank on Day 0 being close to the average influent value of  $0.052 \pm 0.002$  ( $n = 26$ ), decreasing through Phase C but (unlike with sulfate concentrations) not completely rebounding to influent values in Phase F.

As can be seen in Figure 4, perchlorate treatment started on Day 65 and continued throughout the experiment (influent =  $10.7 \pm 0.8$  mM,  $n = 11$ ). In Phase D, concentrations in the tank reached a high of 4.4 mM (Well 11 Day 79) before decreasing to 0 by the end of Phase E (shut-in, Day 124) for all wells, although in some wells perchlorate disappeared earlier (e.g., by Day 89 in Well 6). After shut-in (Phase F), perchlorate concentrations climbed steadily at all locations, reaching an average of  $7.9 \pm 0.6$  mM ( $n = 6$ ) by Day 182. Acetate was added from the point of inoculation (Day  $-16$ ) onward (influent =  $10.9 \pm 1.2$  mM,  $n = 26$ ). After inoculation, acetate was highest close to the influent point (4.5 mM in Well 1, 4.1 mM in Well 2, 1.4 mM in Well 3), reflecting the distance the inoculant traveled into the tank, displacing and mixing with the existing tank pore water. In general, concentrations were low during Phases C–E with mean values less than 0.6 mM ( $n = 12$ ) (Figure 4B), showing close to complete consumption of this electron donor. However, after restarting flow in Phase F, acetate concentrations increased steadily, reaching an average of  $2.1 \pm 0.9$  mM ( $n = 6$ ) on Day 182 and a high of 4.5 mM recorded in Well 10 on Day 153.

The effect of microbial sulfate reduction on the sulfate  $\delta^{34}\text{S}$  value is shown in Figure 4C. Figure 4C shows the temporal trends of  $\delta^{34}\text{S}$  values of sulfate, measured at influent and at Wells 5 and 11, for Phase A–D. Influent  $\delta^{34}\text{S}$  values of sulfate for this period averaged,  $20.7 \pm 0.1$  ‰ ( $n = 15$ ), close to 21‰, a typical value for seawater. In Phase C (souring),  $\delta^{34}\text{S}$  values of Well 5 (Well 11) began to deviate from the influent values between Day 14 (Day 14) and Day 30 (Day 20), and eventually rose to peak values of  $\sim 30$ ‰. The largest shift in  $\delta^{34}\text{S}$  (from influent values) in both wells occurred concurrently



with the rise of sulfide concentrations in the system. In Phase D (sweetening), measured  $\delta^{34}\text{S}$  (at Wells 5 and 11) values decreased toward influent value (of 21‰). At the same time, sulfide concentration fell as sulfate concentration rose.

During souring, black coloration of the sediments in the tank was observed and was attributed to the formation of FeS precipitates (Figure 5B). Dissolved iron concentrations in the tank before inoculation were as high as 1 mM (Figure 5C). Dissolved iron concentrations decreased rapidly by 2 orders of magnitude before the rise of sulfide concentrations (Figure 5C). Thereafter, the dissolved iron concentrations remained low through the rest of the experiment. Figure 5D shows the spatial distribution of solid phase iron at the end of the experiment with much higher concentrations close to the influent. Measurements from the Ottawa sand represent background iron, which was  $\sim 67$  ppm and consistent with value from previous work. (67) Iron content for total iron (6 M HCl digest) varied between 69 and 600 ppm. Bioavailable iron (0.5 M HCl digest) was lower than total iron and varied between  $\sim 200$  ppm to 67 ppm (Figure 5D).

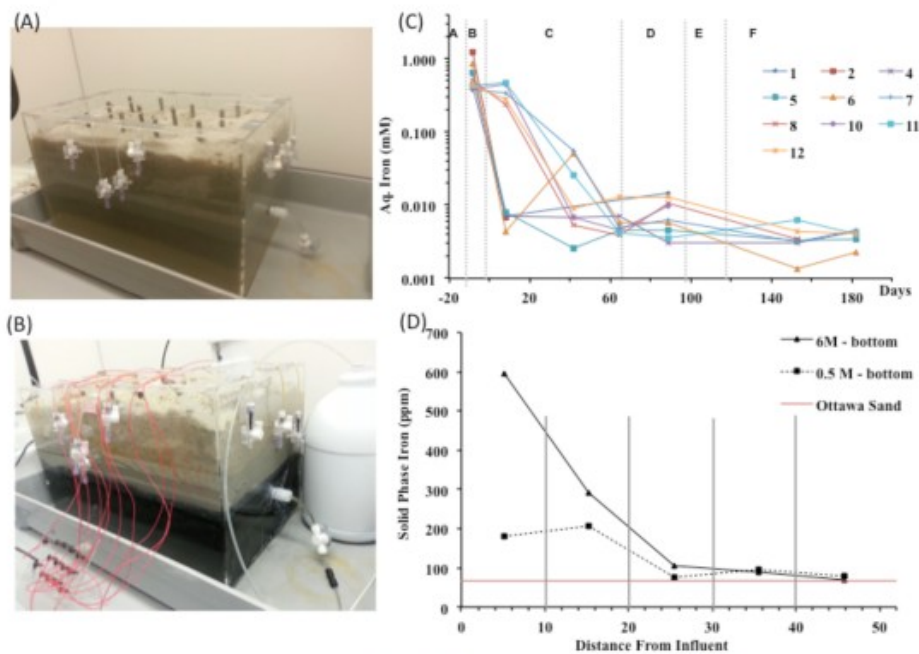


**Figure 5.** Iron in the experiment. Color change before and after sulfidogenesis. (A) Tank before sulfidogenesis, (B) tank with black FeS. (C) Aqueous iron concentration over time. (D) Solid phase iron after experiment: solid black line (bioavailable iron, 0.5 M HCl digest), dashed black line (total iron, 6 M HCl digest).

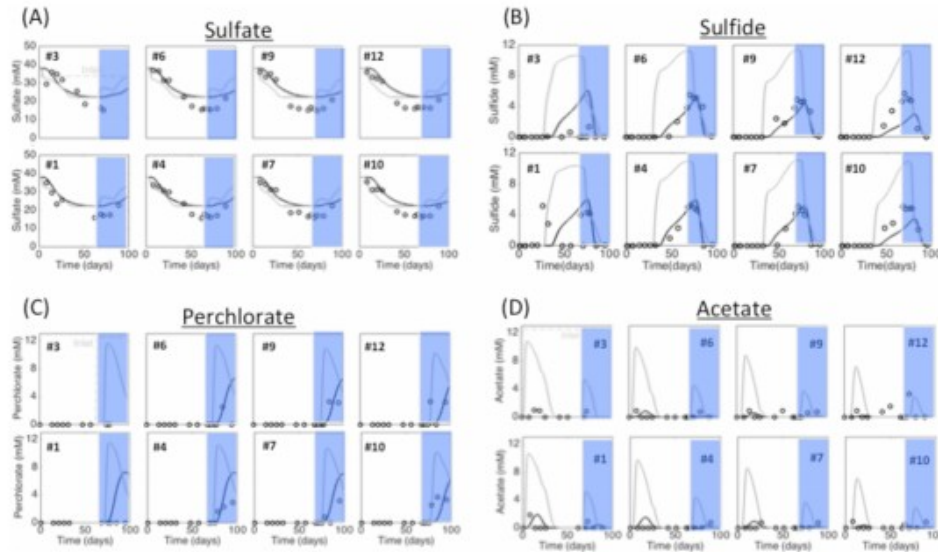


**Figure 6.** (A–D) Observed data (dots) and simulations (heterogeneous model: black line, homogeneous model: gray line) of key chemical species (sulfate, sulfide, and perchlorate) at selected wells (i.e., Wells 2, 5, 8, and 11 removed).

Overall, in the heterogeneous scenario, simulated chemical concentration profiles in the 12 wells reproduce the observed trends in the tank experiment (Figure 6). During souring (Phase C), the model was able to capture the drop (rise) in sulfate (sulfide) concentration as observed in all 12 wells (Figure 6A, 6B). With the exception of Well 3, the model also was able to accurately capture the initial minor pulse of acetate as detected in several wells in the tank (Figure 6D). In the experiment, perchlorate addition began on Day 65 (Phase D). While the model was able to capture the rise in perchlorate concentration in all 12 wells, it tended to overestimate the perchlorate concentration (Figure 6C). Observed perchlorate concentration at all sampling locations were  $\sim 5$  mM, while simulated concentrations were  $\sim 2.5$  mM higher, at 7.5 mM. Simulated sulfide and sulfate showed good agreement with the measured values during this perchlorate addition period (Phase D). Simulated sulfide rapidly dropped from peak value of  $\sim 3$ –5 mM to zero between days 69–78 in response to the injection of perchlorate. Simulated sulfide concentration showed a decreasing trend from the influent to effluent. As a result, the model underestimated sulfide concentration (by  $\sim 1$ –2 mM) at the last row of wells (closest to effluent).

Simulation results from the homogeneous scenario (gray lines) do not match the observed data well. During souring (Phase C), the homogeneous model tends to overestimate sulfate reduction rates, as shown by the lower (higher) simulated sulfate (sulfide) concentrations. Simulated sulfide rose sharply between Days 22–42 to peak values of  $\sim 10$  mM. The model also predicted much higher concentration in the initial acetate peak, 6–10 mM. During souring (Phase D), the model overpredicted perchlorate concentrations in all the wells,  $\sim 10$  mM.

### 3.2.2. Spatial Distribution of Biogeochemical Species

Figure 7 shows the development of the spatial distribution of aqueous sulfide within the tank system, which revealed heterogeneity within the porous media. On Day 8 it was observed that the sulfide front, albeit low in concentration (0.01–0.03 mM), propagated outward from the bottom left of the tank (bird's eye view). As time progressed, the sulfide front propagated further into the system diagonally (from the bottom left corner toward the top right corner). With time, the tank continued to sour, and by Day 65 (the beginning of perchlorate injection), sulfide concentrations within the tank were uniform at ~5 mM. The injection of perchlorate when sulfide concentrations within the tank were uniform offered a chance to observe if flow patterns in the tank remained similar to the souring period. With the addition of perchlorate, sulfide concentrations began to fall, similarly starting from the bottom left corner of the tank. With time, sulfide concentrations within the tank fell, following a gradient: lower sulfide concentration at the bottom right corner, higher concentration at the remaining corners. By Day 89, sulfide concentrations were below 1 mM throughout the tank and below the sulfide detection limit for the majority samples. On Day 106 (during shut-in), sulfide concentration of ~2 mM was detected in the bottom (sampling) layer of the tank. After the shut-in period, as sulfate reduction resumed, sulfide generated in the top layers were transported to the sampling layer and sulfide concentration increased to ~3 mM at the end of experiment.

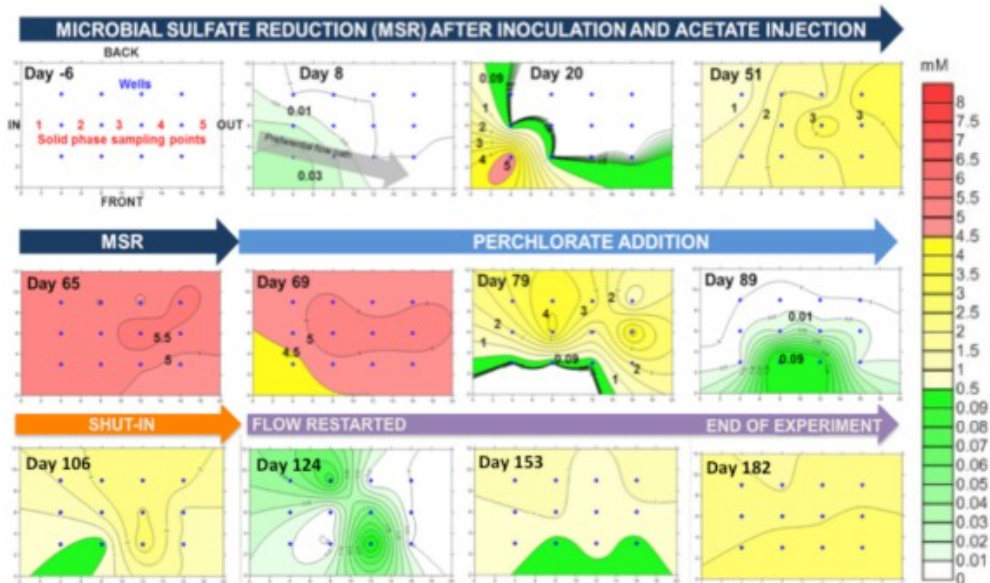
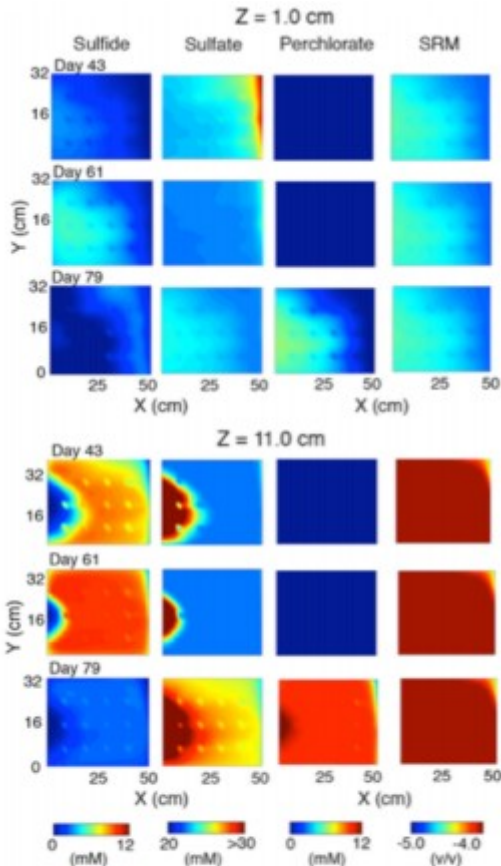


Figure 7. Spatial plots of sulfide through time showing evidence of spatial heterogeneity. The dissolved sulfide data (at  $z = 1$  cm) above show evidence of preferential flow pathways developing during souring and desouring.

Simulated concentration profiles of key chemical species throughout the whole tank with time provide a more complete picture of the coupling between flow, transport, and geochemical processes. First, we follow the concentration profiles of chloride, a nonreactive species (Figure

S2, Supporting Information). Initial chloride concentration in the tank was set at 700 mM (red color in plots), while chloride concentration in injection fluid was 650 mM (blue color in plots). At Day 9, simulations showed that the chloride front moved from left (influent) to right (effluent) (Figure S2, Day 9). The nonuniform shape of the front reflected the heterogeneity in permeability. Since the influent (and effluent) point was at layer  $z = 11$  cm ( $z = 0$  at the bottom of the tank,  $z$ -axis increases as we go up the tank), the chloride front moved through the top layers first. With time, chloride was transported to the bottom layers. At Day 9, chloride from the injection fluid began to propagate into the bottom layers ( $z = 1$  cm). Beyond Day 50, the chloride concentration profile throughout the tank remained steady at 650 mM (Figure S2, Day 69). Chloride shows more preferential flows through the top layers, mainly due to much lower permeability in the  $z$  direction and the location of the injection point.

Comparison of the reactive and nonreactive species can provide information on the extent of reactions that occurred within the tank. On Day 9, simulated sulfate (Figure S2) showed similar patterns to that of chloride: sulfate from the injection fluid was beginning to propagate into the deep layers. These patterns suggested that sulfate reduction was not significant at this time. At Day 69, while the chloride plume had almost covered the whole tank, the magnitude and extent of the sulfate plume had noticeably decreased. In the top layers ( $z = 11$  cm), sulfate concentration gradient ( $\sim 40$ – $30$  mM) could be observed from the left to the right. The magnitude and extent of the sulfate plume decreased with depth (as  $z \rightarrow 1$  cm). Simulations suggested that sulfate reduction rates had increased significantly in the top ( $z = 11$  cm) left segment of the tank. Analysis of the sulfide concentration profiles (Figure S2) corroborates the sulfate simulations. At Day 9, no sulfide was produced in the simulation. With time, sulfate reduction rates increased. In the top layers, sulfate reduction proceeded at a faster rate than in the bottom layers, generating sulfide, which was then transported to the bottom layers. At Day 43, little to no sulfide was observed in the last layer ( $z = 1$  cm) in the simulation (Figure 8).



**Figure 8.** Simulated spatial distribution of aqueous chemical species (sulfate, sulfide, perchlorate) concentration and SRM at the top ( $z = 11$  cm) and bottom ( $z = 1$  cm) layers, and at time points (Days 43, 61, and 79).

At Day 65, perchlorate injection began. Simulated perchlorate (Figure 8) showed similar patterns to that of sulfate and acetate. Up to Day 79, it could be seen from the simulation that perchlorate from the injection fluid was beginning to propagate into the bottom layers. The sulfide concentration profile showed an inverse relationship to the perchlorate concentration profiles. In locations where perchlorate concentrations were high, sulfide concentrations were low (Figure 8). In all, the spatial distributions of reactive aqueous biogeochemical species demonstrate that reactions on top layers occur more significantly than in the bottom layers. In addition, the spatial patterning also suggests that the souring and sweetening processes occur mostly in the high permeability zones.

Figure 8 also shows the spatial distribution of sulfate reducers during the souring phase (Days 43 and 61) as predicted by the model. With time, sulfate reducers grew and progressively expanded into the tank, accumulating mostly close to the injection point and in the high permeability regions (Figure 8). Initial volume fractions of  $C_5H_7O_2N_{SRB}$ ,  $C_5H_7O_2N_{FeRB}$ , and  $C_5H_7O_2N_{PRB}$  are at the order of  $10^{-5}$ , corresponding to a cell density between  $4 \times 10^4$  to  $2 \times 10^6$  cells/mL of the sediment.(60) After 43 days, the volume

fraction of microbes increases to  $\sim 10^{-3}$  (only  $C_5H_7O_2N_{SRB}$  shown in Figure 8), indicating an increase of over 2 orders of magnitude for total cell densities. This is similar to the experimental observation with an increase of cell densities from  $\sim 10^5$  to  $\sim 10^8$  cells/mL. Simulation results also correspond to experimental observations that cell densities from soil samples can be over 1 order of magnitude higher than that from liquid samples (Figure. 9). Figure S3 (Supporting Information) shows the spatial distribution of simulated elemental sulfur (A) and FeS (B) volume percentage during the sweetening phase (Day 69). Elemental sulfur is a product of PRSO (Table2, Rxn 4) and that of the abiotic reduction of Fe(III) by S(-II) (Table2, Rxn 5). In the top layer ( $z = 11$  cm), starting from the influent, elemental sulfur showed a small rising trend (in the  $y$  direction), and thereafter a decreasing trend toward the effluent of the tank. FeS showed similar spatial pattern to elemental sulfur but in lower magnitude. On the basis of the simulation, the sum of precipitates and biomass displayed spatial heterogeneity, with the highest values closest to the influent and in the top layers, around 1.0% by volume of local pore space. This volume is small relative to the pore volume ( $\sim 40\%$ ). According to the potential relationship between porosity and permeability,(66) a porosity decrease of 1.0% may only lead to the decrease of local permeability less than 4.0%. This suggests little alternation of flow paths.

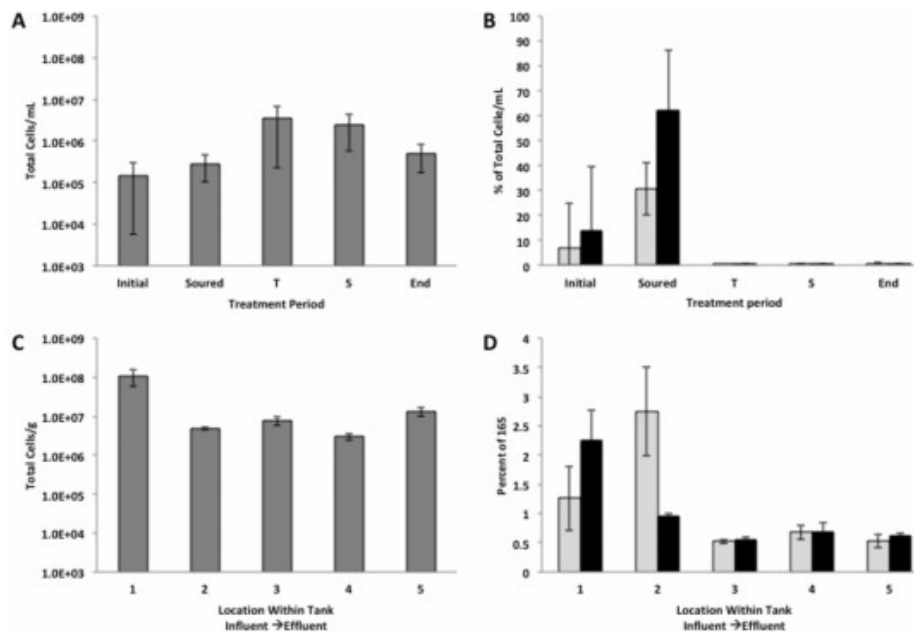


**Figure 9.** qPCR results from liquid and solid samples for (A, C) total cells using general 16S primers and assuming 3.55 copies 16S rRNA gene per cell or for (B, D) quantification of *dsrA* genes using two different sets of primers and represented as a percent of the total cells/mL. "Kondo" primers are represented by gray bars, and "Chin" primers are represented by black bars. Both primer sets assume 1 copy of the *dsrA* gene per cell. Panels A and B represent liquid samples pulled at different time points throughout the experiment with "Initial" samples taken before the tank was soured; "Soured" samples taken after maximal sulfide production was detected; "T" samples taken after perchlorate treatment began; "S" samples taken after the shut-in period; and "End" samples taken when the tank was dismantled. Error bars represent the standard deviation of 6–12 samples taken from across the tank. Panels C and D represent solid samples taken from within the tank when it was dismantled. Locations are represented by a number between 1 and 5 with 1 being closest to the influent port and 5 being closest to the effluent port. Error bars represent the range of duplicate samples.

### 3.3. Microbiology

The qPCR results indicate that the overall microbial abundance changes throughout the experiment. Specifically, the perchlorate-treated samples were significantly different from both the initial and soured samples but were not significantly different from the post shut-in and final samples (ANOVA,  $p = 0.0060$ ,  $\alpha = 0.05$ , Tukey's multiple comparisons, Figure 9A). The abundance of DSR genes as assessed by both primer sets show the same trend, with the soured samples having a higher percentage of organisms with the DSR gene than all other sampling points, indicating that these time points also likely had the highest level of SRM activity (Figure 9B). The SRMs also appear to be nearly eradicated in all samples taken post perchlorate treatment. From the solid samples acquired across the tank at the end of the experiment, a trend of higher abundance of organisms near the influent and lower abundance across the rest of the tank emerges (Figure 9C). However, with only duplicate samples, no statistical tests can be performed. The trend indicates that the highest levels of SRMs are near the influent with lower levels seen closer to the effluent.

The overall microbial community undergoes dramatic changes due to souring and subsequent treatment, with solid and liquid samples grouping separately (Figures S4 and 10). The initial sample is dominated by *Gammaproteobacteria* (28.5%), *Fusobacteria* (19.9%), *Alphaproteobacteria* (18.6%), *Lentisphaerae* (15.9%), and *Deltaproteobacteria* (10.2%). After souring the *Deltaproteobacteria* became enriched to 43.4% of the community, which is unsurprising as they are the dominant group responsible for sulfate reduction. *Bacteroidetes* and *Tenericutes* were also enriched but unlikely to be performing sulfate reduction (Figure 10A). After approximately 20 days of perchlorate treatment, there was enrichment of a single *Sulfurimonas* OTU (*Epsilonproteobacteria*) with abundance reaching  $40.5 \pm 10.7\%$  of the total microbial community. The abundance did fall to  $13.5 \pm 5.8\%$  after the shut-in period, but remained enriched compared to pretreatment, where this organism constituted less than 0.1% of the total community.

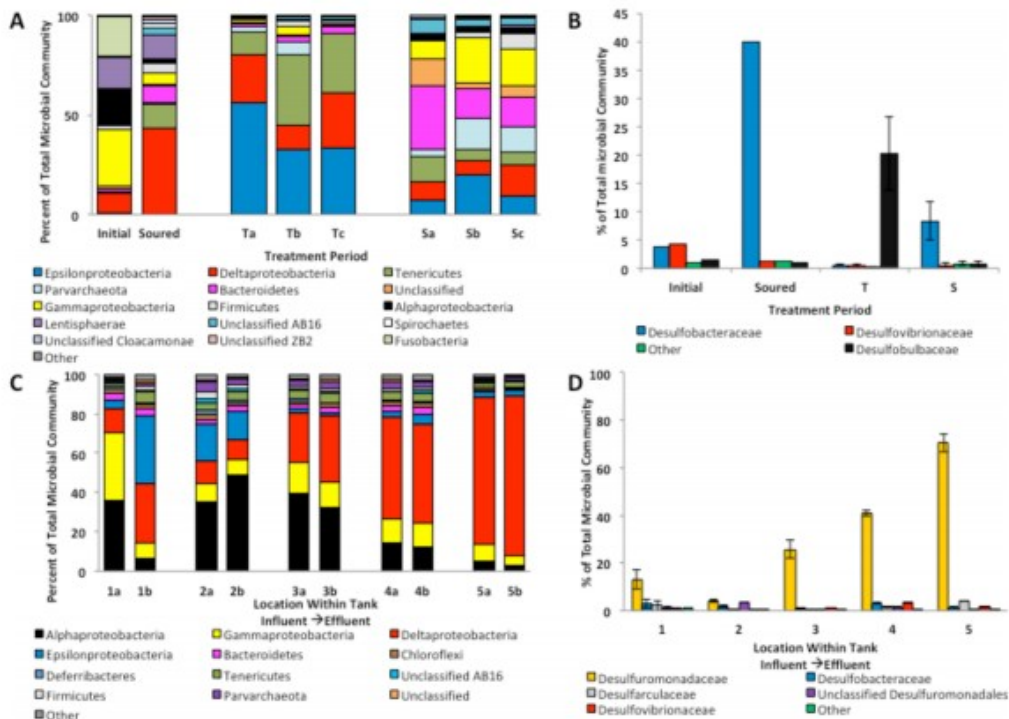


**Figure 10.** Microbial community results. (A) The entire community present in the liquid effluent samples with every OTU representing less than 1.0% abundance in any sample summed into the "other" category. Colored bars represent the phylum or, for Proteobacteria, the class. Initial is a sample taken before the tank was soured; the soured sample was taken after maximal sulfide production was detected; Ta, Tb, and Tc are triplicate samples taken after perchlorate treatment began; and Sa, Sb, and Sc are triplicate samples taken after the shut-in period. (B) Families of sulfate reducing *Deltaproteobacteria* in the liquid samples. Error bars represent the standard deviation of triplicate samples for T and S samples. (C) The entire community present in the solid samples from the final experimental time-point with every OTU representing less than 1.0% abundance in any sample summed into the "other" category. Colored bars represent the phylum or, for Proteobacteria, the class. Location within the tank is represented by a number between 1 and 5 with 1 being closest to the influent port and 5 being closest to the effluent port, and (D) Families of sulfate reducing *Deltaproteobacteria* from this same final experimental time point. Error bars are the range of duplicate samples.

*Deltaproteobacteria*, a class which contains the majority of the sulfate reducing organisms also changed in structure due to treatment (Figure 10B). (12) Initially the sulfate reducing groups *Desulfovibrionaceae* and *Desulfobacteraceae* were found in relatively equal abundance at 4.2% and 3.7% respectively. *Desulfobulbaceae*, a group responsible for a variety of sulfur cycling metabolisms such as  $S^0$  disproportionation, autotrophic  $H_2S$  oxidation, or sulfate reduction, (12,68) initially only represents 1.5% of the total community. After the souring period, *Desulfobacteraceae* jumped to 39.8% of the community, while the other two groups remained around 1% of the total community. However, after perchlorate treatment, *Desulfobacteraceae* was nearly eradicated to only  $0.6 \pm 0.2\%$  of the total community, and *Desulfobulbaceae* was enriched to  $20.2 \pm 6.5\%$ . The one OTU responsible for the majority of this group is unclassified, so it is unclear from this data which metabolic role it is performing. However, the qPCR data indicate only low numbers of DSR genes, and there is very little sulfide detected during this time, so it is unlikely they are performing sulfate reduction. It is more likely they are performing  $S^0$  oxidation since perchlorate reduction in the presence of sulfide is known to produce elemental sulfur. (7,8,12) After the shut in phase, the *Desulfobacteraceae* rebounded to  $8.3 \pm$



3.3% of the community and the *Desulfobulbaceae* fell to  $0.7 \pm 0.6\%$  of the total community.

When the tank matrix was sampled after the experiment, a very different microbial community dominated by *Proteobacteria* (*Delta*, *Gamma*, *Alpha*, and *Epsilon*) was found, and a couple of interesting spatial trends emerged (Figure 10C). *Desulfuromonadaceae* was the dominant sulfur cycling group seen, and its members are primarily known for their ability to reduce  $S^0$ . It increased in abundance in the samples farther from the influent port, with it comprising  $70.5 \pm 3.8\%$  of the total microbial community at the sampling point nearest the effluent. Families responsible for sulfate reduction (*Desulfovibrionaceae*, *Desulfobacteraceae*, and *Desulfarculaceae*) are found in abundances of less than 5% throughout the tank. The same perchlorate reducing *Sulfurimonas* OTU seen in liquid samples after perchlorate treatment was found across the tank in abundances ranging from 0.7% to 34.1% of the total community, with higher abundances seen closer to the influent port and lower abundances seen closer to the effluent port.

## 4. Discussion

### 4.1. Souring and Sweetening Mechanism as Revealed by Experimental Data

Laboratory scale experiments exploring souring and perchlorate treatment are typically simplified homogeneous systems, i.e., microcosms, flow-through columns.(6–8,12,13) In this work, we conducted, to our knowledge, the first mesoscale 3D tank experiment exploring souring and perchlorate treatment.

Experimental observations during the souring phase (Phase C) are comparable to those from the Druhan et al.(62) large column study. The 1 m column experiment was set up as a comprehensive model of sulfur cycling and  $\delta^{34}S$  fractionation processes occurring in a uranium contaminated aquifer, and generated high resolution spatial and temporal data pertaining to dissimilatory sulfate reduction (DSR). While 10 mM acetate was also added as carbon source, influent sulfate and salinity in the artificial groundwater in Druhan et al.(62) were lower in comparison to those used in this study (from seawater). However, given the ubiquitous nature of DSR (e.g., souring has been shown to occur in freshwater, brackish and saline conditions, though with different SRM profiles(69)), comparison of our results to those from Druhan et al.(62) remains useful. Below we discuss a few key similarities.

It is worth noting the delays in the timing of the sulfide breakthrough in comparison to that of the  $\delta^{34}S$ . Sulfide began to significantly increase due to souring beyond ~ Day 25 (Day 40 for Well 5) (Figure 4), ~10 days after increased  $\delta^{34}S$  of sulfate. The delay in sulfide breakthrough has also been observed in other field(70) and column studies,(62) and was attributed to the occurrence of iron mineral-sulfide reactions. Together with these studies, data from this work affirm the use of  $\delta^{34}S$  of dissolved sulfate as a more

accurate proxy than sulfide for the onset of sulfate reduction when the mineral matrix can scavenge dissolved sulfide.(62,70,71)

During souring, black coloration of the sediments in the tank was observed and attributed to the formation of FeS precipitates (Figure 6B). Similar black precipitates (in the form of FeS) were also observed in Druhan et al.(62) In addition, they noted the FeS were lost during the excavation process, most likely due to reoxidation. Yellow precipitates (image not shown), presumably elemental sulfur, were observed in the tank during the experiment. In Druhan et al.,(62) measured solid phase elemental sulfur at sampling points throughout the length of the column revealed a decreasing trend from the influent (300 ppm) to the effluent (50 ppm). Simulated elemental sulfur in the same study also showed a similar trend. While elemental sulfur was not quantified in our experiment, visual observations and microbial community analysis (to be discussed) lend support to its presence. Below we also discuss its spatial pattern as simulated by reactive transport model.  $S^0$  was also observed in earlier perchlorate treatment column studies, however, its formation was attributed to both abiotic and biotic pathways.(12,13) In the abiotic pathway, elemental sulfur forms when iron oxide minerals are reduced in the coupled redox reaction with sulfide. In the biotic pathway, elemental sulfur forms when a perchlorate reducing microbial population couples the reduction of perchlorate to the oxidation of sulfide.(7,8)

In this study, trends in the geochemical data coupled with the microbial community analysis yield insights as to the different mechanisms by which perchlorate inhibits sulfate reduction. As a direct inhibitor of the central sulfate-reduction pathway,(6) perchlorate immediately suppressed the sulfate reducing community in the tank, causing reduction in sulfide concentrations while perchlorate concentrations were still increasing. Perchlorate was detected with concentrations peaking in most of the wells 7–14 days after applications (Days 72–79). It is also noted that during the same time, (Day 65–79), sulfate concentration plateaued. This was accompanied by a decrease in sulfide, which indicates a loss of total measurable sulfur mass and suggest possible precipitation of  $S^0$  through PRSO.(13) However, we were not able to determine the relative magnitude of the two inhibiting mechanisms.

The microbial community analysis indicates *Desulfobacteraceae* are likely the primary group responsible for sulfide generation during the souring phase before perchlorate treatment commenced (Figure 10B), and the presence of large numbers of SRM genes during this time supports the geochemical results. However, after perchlorate treatment, the *Desulfobacteraceae* population was significantly reduced. This result is consistent with a previous study in which perchlorate inhibited the sulfate reducing families *Desulfobacteraceae*, *Desulfovibrionaceae*, and *Desulfomicrobiaceae*.(12) After the initial effects, between Day 79 and Day 89, sulfate concentrations rebounded with a concurrent decrease in sulfide concentrations and increase in perchlorate concentrations. These

trends suggest that the action of the third inhibition mechanism, biocompetition, is suppressing sulfidogenesis. Indeed, the microbial analyses indicated that after approximately 20 days (Day 85) of perchlorate treatment there was enrichment of a single *Sulfurimonas* OTU. During the treatment phase, *Sulfurimonas* dominated and is likely performing heterotrophic perchlorate reduction in this system.(72)

Microbial community analysis also provided some clues to the organisms responsible for the sulfide that was detected during shut-in. It was noted that after the shut in, *Desulfobacteraceae* rebounded. It is likely that during shut-in, with no fresh perchlorate injected, perchlorate concentrations within the tank fell to a level that was less toxic to the sulfate reducing community, allowing their populations to rebound and sulfate reduction resumed. Furthermore, the community analysis provided possible explanations for the rebound of sulfide in the last phase of the experiment, despite the continued perchlorate injection. It was noted that obligate  $S^0$  reducing families (*Desulfuromonadaceae*)(73,74) were enriched in the last phase of the experiment. Engelbrekton et al.(12) also showed that (per)chlorate treatment enriched for *Desulfuromonadaceae* and suggested they were involved in redox cycling sulfur between  $H_2S$  and elemental sulfur—specifically, the generation of sulfide as mediated by *Desulfuromonadaceae*, which would in turn be oxidized back into elemental sulfur by the perchlorate reducers through PRSO. The utilization of the PRSO pathway preferentially by the perchlorate reducing community meant no growth in biomass. With no biomass growth, the perchlorate-reducing community could not remain competitive against the sulfate/sulfur reducing community for electron donor, further reducing the inhibitive impact of perchlorate. The utilization of the PRSO pathway also could explain the rising perchlorate concentrations, since PRSO consumes less perchlorate than heterotrophic perchlorate reduction: reduction of 1 mol of perchlorate coupled to oxidation of 4 mol of sulfide, compared to reduction of 1 mol of perchlorate coupled to oxidation of 1.25 mol of acetate.

#### 4.2. Reactive Transport Modeling

We developed a reactive transport model of souring and subsequent perchlorate treatment in the mesoscale tank using the comprehensive data set generated. Microbial analysis and geochemical data indicated the presence of two inhibition mechanisms in the early days following perchlorate addition: direct toxicity and competitive inhibition due to the presence of PRSOs. The relative magnitude of the two inhibiting mechanisms, however, was challenging to quantify. An additional simulation was conducted in which the direct inhibitory impact of perchlorate on sulfate was alleviated by setting the value of  $K_{inhibitor}$ , the perchlorate inhibition constant of the SRM, to an order of magnitude higher ( $1.9 \times 10^{-2}$  mol/L) than the original simulation ( $1.9 \times 10^{-3}$  mol/L). The higher  $K_{inhibitor}$  value is within the range as revealed by the Carlson et al.(6) study. With the direct inhibitory effect alleviated, simulated sulfide concentrations increased in all

wells, a clear departure from the original simulation, in which sulfide concentrations fell to zero in response to perchlorate injection (Figure S5, Supporting Information). Simulated perchlorate trends remained similar between the two sets of simulations, indicating little consumption of perchlorate through the PRSO mechanism, and suggesting that direct toxicity is the dominant mechanism. In recent flow through column experiments, Wu et al.(13) and Engelbrektson et al.(14) also identified toxicity impact of perchlorate as the dominating mechanism contributing to the initial drop in sulfate reduction rates.

In this study, experimental data suggest the presence of a diverse sulfur cycling community emerging in situ, which is made up of different sulfate reducing families (e.g., *Desulfobulbaceae*, *Desulfobacteraceae*), each with different physiologies and responsible for different sulfur cycling metabolisms. A simplified representation of the kinetics of sulfate reducing microorganism, common across many modeling studies, works well during the souring and sweetening phases in this work, most likely because the conditions were selecting for a dominant microbial population/guild (either SRM or PRM during the souring and sweetening phases respectively). As a case in point, in this work, during souring, *Desulfobacteraceae* was enriched over other families of SRMs initially present. However, the model may not be able to capture the system dynamics during the shut in and final phase of the experiment. Perchlorate enriches for organisms mediating different pathways in the sulfur cycle:(12,14) examples are *Desulfuromonadaceae* (a known  $S^0$  reducer) and *Desulfobulbaceae* (sulfate reduction,  $S^0$  disproportionation and autotrophic  $H_2S$  oxidation). The result is a decrease in abundance of the canonical SRM population, reducing sulfate reduction but stimulating sulfur cycling. To better capture the dynamics of the microbial community, future numerical models should incorporate microbes mediating other key pathways in the sulfur and perchlorate cycles. Specifically, as echoed in our earlier studies,(31,32) we suggest the incorporation of a trait based modeling (TBM) approach into the RTM framework (e.g., BioCrunch(75)). In TBM, complex microbial communities are represented by metabolically/functionally important groups (guilds), each defined by a collection of physiological traits.(76,77) In addition, experimental sampling should include data that will help constrain the kinetics of the newly incorporated microbes (e.g.,  $S^0$ ).

#### 4.3. Impacts of Heterogeneity

Comparisons between the homogeneous and the heterogeneous simulation highlighted the role of permeability ratio of  $k_x$ ,  $k_y/k_z$  (i.e., anisotropy) in controlling reactive transport. In the heterogeneous case, the permeability ratio  $k_x/k_z > 1.0$  leads to higher horizontal fluxes than vertical fluxes. However, in the homogeneous case where  $k_x = k_y = k_z$  (regardless of the magnitude of  $k$ , e.g.,  $10^{-10}$  or  $10^{-12}$   $m^2$ ) the proportion of water flowing through each direction is fixed by permeability ratio ( $k_x/k_z$  and  $k_y/k_z = 1.0$ ). The use of a homogeneous simulation domain failed to capture the

breakthrough data of the nonreactive tracers (fluorescein and bromide, gray lines in Figure 2). In the homogeneous case, because the permeability contrast  $k_z/k_x (= k_y)$  was almost a magnitude higher compared to that in the heterogeneous case, earlier and higher dissolved chemical species signals were predicted due to faster infiltration of dissolved chemical species into the deeper layers (where the sampling ports are located). The impact of vertical flow was also evident in the fluorescein simulations, in which the homogeneous effluent signal showed up later and lower in magnitude than the heterogeneous case. We can also attribute the late arrival and reduced magnitude to loss of fluorescein to deeper layers. In other words, the anisotropy (also a reflection of heterogeneity) determines how much water flowed horizontally or vertically.

Our results show that the spatial distribution of permeability plays a role in determining the distribution of abiotic precipitates and microbial population. Spatial distribution of simulated elemental sulfur, FeS (Figure S3) and SRM (Figure 8) follow a general pattern of higher levels near the influent with lower levels seen closer to the effluent. Similar patterns were also observed in previous studies on bioreduction in both the laboratory(62) and at the field scale.(60) Elemental sulfur is a product of PRSO (Table2, Rxn 4) and that of the abiotic reduction of Fe(III) by S(-II) (Table2, Rxn 6). In the top layer ( $z = 11$  cm), starting from the influent, elemental sulfur showed small rising trend (in the  $y$  direction, along length of tank), and thereafter a decreasing trend toward the effluent of the tank. Such a pattern was also observed in the column of Druhan et al.,(62) a rising trend (200 to 300 ppm) in the first 20 cm of the column, then a decreasing trend (300 to 50 ppm) in the remaining column. This initial limited zone of low elemental sulfur corresponds to the zone where sulfide concentrations were insignificant. Li et al.(60) showed that in the field, SRM biomass tend to be at higher concentrations near the injection wells than the extraction wells. However, a notable difference between this study and the 1D column study is the observation that the distribution of the minerals and microbial population also bear general resemblance to the permeability field (Figure 8), with accelerated growth in the zone of preferential flow path. The preferential growth can be attributed to higher delivery rates of electron donor and acceptor to microbes in the region.

Studies have shown that biogeochemical processes take place favorably at intersections between high contrast regions (e.g., interface between high perm into low perm).(25,60,78–80) Interfacial regions between zones covering a transition from coarse-to-fine grain sizes have been found to promote organic matter degradation and biomass growth.(80) In our simulation, we did not observe enhanced mineral and biomass growth at the transitional regions between the high and low permeability zones (in the  $x$ - $y$  plane). In the investigation of the impact of spatial patterning of magnesite on dissolution rates in flow through columns, Salehikhoo and Li(79) showed that spatial patterning of the minerals interact with flow velocity and

permeability contrast to determine dissolution rates. Therefore, in our study, the lack of enhanced mineral and biomass growth at the transitional region between high and low permeability zones is likely due to the low permeability contrast: permeability field (x-y plane) range from  $1-5 \times 10^{-10} \text{ m}^2$ . This low degree of permeability contrast most likely occurred during the process of packing. In a reactive transport modeling study by Li et al. (60) magnesite and calcite formed at the interface between conductivities  $10^{0.84}$  and  $10^{-0.4} \text{ m day}^{-1}$ , values that were at least an order of magnitude apart.

The control that spatial distributions of hydrologic characteristics exert on reservoir souring and treatment, as revealed in this mesoscale system, has implications for understanding and predicting souring in oil reservoirs. Oil bearing geological formations are characterized by distinct zones of mineralogy. Each zone can differ from the other in permeability by orders of magnitude. Therefore, spatial heterogeneities are likely to exert significant control over microbial activities in oil reservoirs. Further, in oil bearing fractured rock systems, fractures act as preferential flow pathways, controlling transport of water and dissolved nutrients, and subsequently, the spatial distribution of microbes. Microbial biomass tends to form biofilms at the interface between fracture and matrix, where they experience diffusion limitation in the nutrient acquisition process. Follow up experiments are warranted. Souring and perchlorate treatment in heated fractured rock system is the focus of an ongoing research effort.

## 5. Conclusion

In this study, a novel mesoscale tank experiment is coupled with reactive transport modeling to explore the effects of heterogeneity on souring and perchlorate interventions. The experiment yielded a comprehensive isotopic, water chemistry, and microbial data set that revealed spatial and temporal patterning of processes within the system. Despite the use of similar material in the packing of the target layer, preference flow pathways still emerged, controlling the transport of water with nutrients and impacting spatial distribution of microbial growth and biogeochemical reactions. The high-resolution sampling also provided a rare view into the role of heterogeneity in generating and transporting sulfide throughout the experiment. Model simulations captured the spatiotemporal trends of the key geochemical and microbial species through the souring and sweetening phases. Further comparison between the heterogeneous and homogeneous model results showed that the homogeneous model significantly overestimates the sulfide amount in the system by as much as ~240%. These three-dimensional physical model experiments represent a systematic way of incorporating complexity beyond the batch and column experiments, and exploring the combined effects of heterogeneity (present in the fields) and first order biogeochemical processes (explored in earlier batch and column experiments).

## Acknowledgments

This work was funded by the Energy Biosciences Institute. The authors would like to thank the reviewers for their constructive comments.

## References

- (1) Beauchamp, R. O.; Bus, J. S.; Popp, J. A.; Boreiko, J.; Andjelkovich, D. A.; Leber, P. A critical review of the literature on hydrogen sulfide toxicity. *CRC Crit Rev. Toxicol* 1984, 13 (1), 25–97.
- (2) Reiffenstein, R. J.; Hulbert, W. C.; Roth, S. H. Toxicology of Hydrogen Sulfide. *Annu. Rev. Pharmacol. Toxicol.* 1992, 32 (1), 109–134.
- (3) Fuller, D. C.; Suruda, A. J. Occupationally related hydrogen sulfide deaths in the United States from 1984 to 1994. *J. Occup. Environ. Med.* 2000, 42 (9), 939–942.
- (4) Ollivier, B.; Magot, M. Reservoir Souring: Mechanisms and Prevention. *Pet. Microbiol.* 2016, No. Chapter 7, 123–142.
- (5) Grigoryan, A. A.; Cornish, S. L.; Buziak, B.; et al. Competitive oxidation of volatile fatty acids by sulfate- and nitrate-reducing bacteria from an oil field in Argentina. *Appl. Environ. Microbiol.* 2008, 74 (14), 4324–4335.
- (6) Carlson, H. K.; Kuehl, J. V.; Hazra, A. B.; et al. Mechanisms of direct inhibition of the respiratory sulfate-reduction pathway by (per)chlorate and nitrate. *ISME J.* 2015, 9 (6), 1295–1305.
- (7) Gregoire, P.; Engelbrektson, A.; Hubbard, C. G.; et al. Control of sulfidogenesis through bio-oxidation of H<sub>2</sub>S coupled to (per)chlorate reduction. *Environ. Microbiol. Rep.* 2014, 6 (6), 558–564.
- (8) Mehta-Kolte, M. G.; Loutey, D.; Wang, O., et al. Mechanism of H<sub>2</sub>S oxidation by the dissimilatory perchlorate-reducing microorganism *Azospira suillum* PS. *mBio* 2017, 8(1), DOI: 10.1128/ mBio.02023-16.
- (9) Myhr, S.; Lillebø, B. L.; Sunde, E.; Beeder, J.; Torsvik, T. Inhibition of microbial H<sub>2</sub>S production in an oil reservoir model column by nitrate injection. *Appl. Microbiol. Biotechnol.* 2002, 58 (3), 400–408.
- (10) Hubert, C.; Nemati, M.; Jenneman, G.; Voordouw, G. Containment of biogenic sulfide production in continuous up-flow packed-bed bioreactors with nitrate or nitrite. *Biotechnol. Prog.* 2003, 19 (2), 338–345.
- (11) Kaster, K. M.; Grigoriyan, A.; Jenneman, G.; Voordouw, G. Effect of nitrate and nitrite on sulfide production by two thermophilic, sulfate-reducing enrichments from an oil field in the North Sea. *Appl. Microbiol. Biotechnol.* 2007, 75 (1), 195–203.
- (12) Engelbrektson, A.; Hubbard, C. G.; Tom, L. M., et al. Inhibition of microbial sulfate reduction in a flow-through column system by (per)chlorate treatment. *Front. Microbiol.* 2014, (JUN), DOI: 10.3389/fmicb.2014.00315.
- (13) Wu, Y.; Cheng, Y.; Hubbard, C. G.; Hubbard, S.; Ajo-Franklin, J. B. Biogenic sulfide control by nitrate and (per)chlorate – A monitoring and modeling investigation. *Chem. Geol.* 2018, 476, 180.
- (14) Engelbrektson, A., Cheng, Y., Hubbard, C. G., et al. Attenuating sulfidogenesis in a Sourved Continuous Flow Column System with Perchlorate Treatment, submitted, 2018.
- (15) Jenneman, G.; Moffitt, P.; Bala, G.; Webb, R. Sulfide Removal in Reservoir Brine by Indigenous Bacteria. *SPE Production & Facilities* 1999, 14 (3), 5–8.
- (16) Larsen, J. Downhole nitrate applications to control sulphate reducing bacteria activity and reservoir souring. *Corrosion* 2002, 2002 (02025), 10.
- (17) Larsen, J.; Rod, M. H.; Zwolle, S. Prevention of reservoir souring in the Halfdan field by nitrate

injection. *Corrosion* 2004, 2004 (04761), 18. (18) Vik, E. A.; Janbu, A. O.; Garshol, F.; et al. Nitrate - Based Souring Mitigation of Produced Water ∂ Side Effects and Challenges From the Draugen Produced - Water Reinjection Pilot. *SPE International* 2007, 106178, 1–11. (19) Voordouw, G.; Grigoryan, A. A.; Lambo, A.; et al. Sulfide remediation by pulsed injection of nitrate into a low temperature Canadian heavy oil reservoir. *Environ. Sci. Technol.* 2009, 43 (24), 9512–9518. (20) Magot, M.; Ollivier, B.; Patel, B. K. C. Microbiology of petroleum reservoirs [Review]. *Antonie van Leeuwenhoek* 2000, 77 (1977), 103–116. (21) Sudicky, E. A.; Illman, W. A.; Goltz, I. K.; Adams, J. J.; McLaren, R. G. Heterogeneity in hydraulic conductivity and its role on the macroscale transport of a solute plume: From measurements to a practical application of stochastic flow and transport theory. *Water Resour. Res.* 2010, 46(1), DOI: 10.1029/2008WR007558. (22) Scheibe, T. D.; Hubbard, S. S.; Onstott, T. C.; DeFlaun, M. F. Lessons learned from bacterial transport research at the South Oyster Site. *Groundwater* 2011, 49 (5), 745–763. (23) Li, L.; Gawande, N.; Kowalsky, M. B.; Steefel, C. I.; Hubbard, S. S. Physicochemical heterogeneity controls on uranium bioreduction rates at the field scale. *Environ. Sci. Technol.* 2011, 45 (23), 9959– 9966. (24) Bao, C.; Wu, H.; Li, L.; Newcomer, D.; Long, P. E.; Williams, K. H. Uranium bioreduction rates across scales: Biogeochemical hot moments and hot spots during a biostimulation experiment at Rifle, Colorado. *Environ. Sci. Technol.* 2014, 48 (17), 10116–10127. (25) Wen, H.; Li, L. An upscaled rate law for magnesite dissolution in heterogeneous porous media. *Geochim. Cosmochim. Acta* 2017, 210, 289–305. (26) Meile, C.; Tuncay, K. Scale dependence of reaction rates in porous media. *Adv. Water Resour.* 2006, 29 (1), 62–71. (27) Thullner, M. Comparison of bioclogging effects in saturated porous media within one- and two-dimensional flow systems. *Ecological Engineering* 2010, 36 (2), 176–196. (28) Farhadinia, M. A.; Bryant, S. L.; Sepehrnoori, K.; Delshad, M. Development and implementation of a multidimensional reservoir souring module in a chemical flooding simulator. *Pet. Sci. Technol.* 2010, 28 (6), 535–546. (29) Haghshenas, M.; Sepehrnoori, K.; Bryant, S. L.; Farhadinia, M. A. Modeling and Simulation of Nitrate Injection for Reservoir Souring Remediation. *SPE International Symposium on Oilfield Chemistry* 2012, 17 (September), 817–827. (30) Hosseininoosheri, P., Lashgari, H., Sepehrnoori, K. Numerical Prediction of Reservoir Souring under the Effect of Temperature, Ph, and Salinity on the Kinetics of Sulfate-Reducing Bacteria. In *SPE International Symposium on Oilfield Chemistry*, 2017. (31) Cheng, Y.; Hubbard, C. G.; Li, L., et al. Reactive Transport Model of Sulfur Cycling as Impacted by Perchlorate and Nitrate Treatments. *Environ. Sci. Technol.* 2016, 50(13), 7010. (32) Cheng, Y.; Hubbard, C. G.; Zheng, L., et al. Next generation modeling of microbial souring – Parameterization through genomic information. *Int. Biodeterior. Biodegrad.* 2018, 126, 189. (33) Cline, J. D. Spectrophotometric Determination of Hydrogen Sulfide in Natural Waters. *Limnol. Oceanogr.* 1969, 14 (3), 454–458. (34) Cord-Ruwisch, R. A quick method for the determination of dissolved and precipitated sulfides in cultures of sulfate-reducing bacteria. *J. Microbiol. Methods* 1985, 4 (1),



33–36. (35) Stookey, L. L. Ferrozine-A New Spectrophotometric Reagent for Iron. *Anal. Chem.* 1970, 42 (7), 779–781. (36) Hansel, C. M.; Benner, S. G.; Neiss, J.; Dohnalkova, a.; Kukkadapu, R.; Fendorf, S. Secondary mineralization pathways induced by dissimilatory iron reduction of ferrihydrite under advective flow. *Geochim. Cosmochim. Acta* 2003, 67 (16), 2977–2992. (37) Caporaso, J. G.; Lauber, C. L.; Walters, W. A.; et al. Global patterns of 16S rRNA diversity at a depth of millions of sequences per sample. *Proc. Natl. Acad. Sci. U. S. A.* 2011, 108 (Supplement\_1), 4516–4522. (38) Caporaso, J. G.; Kuczynski, J.; Stombaugh, J.; et al. QIIME allows analysis of high-throughput community sequencing data. *Nat. Methods* 2010, 7 (5), 335–336. (39) Steefel, C. I.; Appelo, C. A. J.; Arora, B.; et al. Reactive transport codes for subsurface environmental simulation. *Computational Geosciences* 2015, 19 (3), 445–478. (40) Rittmann, B. E., McCarty, P. L., Rittman, B. E., McCarty, P. L. *Environmental Biotechnology: Principles and Applications* 2010, 10, DOI: 10.1016/S0958-1669(96)80047-4. (41) Lloyd, J. R. Microbial reduction of metals and radionuclides. *FEMS Microbiology Reviews* 2003, 27, 411. (42) Lasaga, A. C.; Soler, J. M.; Ganor, J.; Burch, T. E.; Nagy, K. L. Chemical weathering rate laws and global geochemical cycles. *Geochim. Cosmochim. Acta* 1994, 58 (10), 2361–2386. (43) Doherty, J. PEST: A Unique Computer Program for Modelindependent Parameter Optimisation. In *Water Down Under 94: Groundwater/Surface Hydrology Common Interest Papers; Preprints of Papers*, 1994, 551, <http://search.informit.com.au/documentSummary;dn=752715546665009;res=IELENG>. (44) Doherty, J. PLPROC - A Parameter List Processor; Queensland, Australia, 2015. (45) Fernandez-Garcia, D.; Rajaram, H.; Illangasekare, T. H. Assessment of the predictive capabilities of stochastic theories in a three-dimensional laboratory test aquifer: Effective hydraulic conductivity and temporal moments of breakthrough curves. *Water Resour. Res.* 2005, 41 (4), 1–14. (46) Post, V. E. A.; Simmons, C. T. Free convective controls on sequestration of salts into low-permeability strata: insights from sand tank laboratory experiments and numerical modelling. *Hydrogeol. J.* 2010, 18 (1), 39–54. (47) Kowalsky, M. B.; Finsterle, S.; Williams, K. H., et al. On parameterization of the inverse problem for estimating aquifer properties using tracer data. *Water Resour. Res.* 2012, 48(6), DOI: 10.1029/2011WR011203. (48) Baeuerle, P. A.; Huttner, W. B. Chlorate—a potent inhibitor of protein sulfation in intact cells. *Biochem. Biophys. Res. Commun.* 1986, 141 (2), 870–877. (49) Postgate, J. R. Competitive and Non-competitive Inhibitors of Bacterial Sulphate Reduction. *J. Gen. Microbiol.* 1952, 6 (1–2), 128–142. (50) Pallud, C.; Van Cappellen, P. Kinetics of microbial sulfate reduction in estuarine sediments. *Geochim. Cosmochim. Acta* 2006, 70 (5), 1148–1162. (51) Porter, D.; Roychoudhury, A. N.; Cowan, D. Dissimilatory sulfate reduction in hypersaline coastal pans: Activity across a salinity gradient. *Geochim. Cosmochim. Acta* 2007, 71 (21), 5102–5116. (52) Jung, J.; Hyun, S. P.; Lee, J. K.; Cho, Y. H.; Hahn, P. S. Adsorption of UO<sub>2</sub><sup>2+</sup> on natural composite materials. *J. Radioanal. Nucl. Chem.* 1999, 242 (2), 405–412. (53) Monod, J.

The growth of bacterial cultures. *Annu. Rev. Microbiol.* 1949, 3 (1), 371–394.

(54) Ratkowsky, D. A.; Olley, J.; McMeekin, T. A.; Ball, A. Relationship between temperature and growth-rate of bacterial cultures. *Journal of Bacteriology* 1982, 149 (1), 1–5.

(55) Kostka, J. E.; Dalton, D. D.; Skelton, H.; Dollhopf, S.; Stucki, J. W. Growth of iron(III)-reducing bacteria on clay minerals as the sole electron acceptor and comparison of growth yields on a variety of oxidized iron forms. *Applied and Environmental Microbiology* 2002, 68 (12), 6256–6262.

(56) Medircio, S. N.; Leao, V. A.; Teixeira, M. C. Specific growth rate of sulfate reducing bacteria in the presence of manganese and cadmium. *J. Hazard. Mater.* 2007, 143 (1-2), 593–596.

(57) Bonneville, S.; Van Cappellen, P.; Behrends, T. Microbial reduction of iron(III) oxyhydroxides: Effects of mineral solubility and availability. *Chem. Geol.* 2004, 212 (3–4 SPEC. ISS), 255–268.

(58) Roden, E. E.; Zachara, J. M. Microbial reduction of crystalline iron(III) oxides: Influence of oxide surface area and potential for cell growth. *Environ. Sci. Technol.* 1996, 30 (5), 1618–1628.

(59) Van Cappellen, P.; Wang, Y. Cycling of iron and manganese in surface sediments: A general theory for the coupled transport and reaction of carbon, oxygen, nitrogen, sulfur, iron, and manganese. *Am. J. Sci.* 1996, 296 (3), 197–243.

(60) Li, L.; Steefel, C. I.; Kowalsky, M. B.; Englert, A.; Hubbard, S. S. Effects of physical and geochemical heterogeneities on mineral transformation and biomass accumulation during biostimulation experiments at Rifle, Colorado. *J. Contam. Hydrol.* 2010, 112 (1–4), 45–63.

(61) Liu, C.; Kota, S.; Zachara, J. M.; Fredrickson, J. K.; Brinkman, C. K. Kinetic analysis of the bacterial reduction of goethite. *Environ. Sci. Technol.* 2001, 35 (12), 2482–2490.

(62) Druhan, J. L.; Steefel, C. I.; Conrad, M. E.; DePaolo, D. J. A large column analog experiment of stable isotope variations during reactive transport: I. A comprehensive model of sulfur cycling and  $\delta^{34}\text{S}$  fractionation. *Geochim. Cosmochim. Acta* 2014, 124, 366–393.

(63) Charlet, L.; Tournassat, C. Fe(II)-Na(I)-Ca(II) cation exchange on montmorillonite in chloride medium: Evidence for preferential clay adsorption of chloride - Metal ion pairs in seawater. *Aquat. Geochem.* 2005, 11 (2), 115–137.

(64) Gelhar, L. W.; Welty, C.; Rehfeldt, K. R. A critical review of data on field-scale dispersion in aquifers. *Water Resour. Res.* 1992, 28 (7), 1955–1974.

(65) Yuan-Hui, L.; Gregory, S. Diffusion of ions in sea water and in deep-sea sediments. *Geochim. Cosmochim. Acta* 1974, 38 (5), 703–714.

(66) Costa, A. Permeability-porosity relationship: A reexamination of the Kozeny-Carman equation based on a fractal pore-space geometry assumption. *Geophys. Res. Lett.* 2006, 33(2), DOI: 10.1029/2005GL025134.

(67) Hubbard, C. G.; West, L. J.; Morris, K., et al. In search of experimental evidence for the biogeobattery. *J. Geophys. Res.* 2011, 116(4), DOI: 10.1029/2011JG001713.

(68) Pfeffer, C.; Larsen, S.; Song, J.; et al. Filamentous bacteria transport electrons over centimetre distances. *Nature* 2012, 491, 218.

(69) Voordouw, G.; Voordouw, J. K.; Jack, T. R.; Foght, J.; Fedorak, P. M.; Westlake, D. W. S. Identification of distinct communities of sulfate-reducing bacteria in oil fields by reverse sample genome probing. *Appl. Environ. Microbiol.* 1992, 58 (11), 3542–3552.

(70) Druhan, J. L.; Steefel, C. I.; Molins, S.; Williams, K. H.;

Conrad, M. E.; Depaolo, D. J. Timing the onset of sulfate reduction over multiple subsurface acetate amendments by measurement and modeling of sulfur isotope fractionation. *Environ. Sci. Technol.* 2012, 46 (16), 8895–8902.

(71) Hubbard, C. G.; Cheng, Y.; Engelbrekston, A., et al. Isotopic insights into microbial sulfur cycling in oil reservoirs. *Front. Microbiol.* 2014, 5(SEP), DOI: 10.3389/fmicb.2014.00480.

(72) Barnum, T. P.; Figueroa, I. A.; Carlström, C. I.; Lucas, L. N.; Engelbrekton, A. L.; Coates, J. D. Genome-resolved metagenomics identifies genetic mobility, metabolic interactions, and unexpected diversity in perchlorate-reducing communities. *ISME J.* 2018, 1–14.

(73) Finster, K.; Bak, F.; Pfennig, N. *Desulfuromonas acetexigens* sp. nov., a dissimilatory sulfur-reducing eubacterium from anoxic freshwater sediments. *Arch. Microbiol.* 1994, 161, 328.

(74) Finster, K.; Coates, J. D.; Liesack, W.; Pfennig, N. *Desulfuromonas thiophila* sp. nov., a New Obligately Sulfur-Reducing Bacterium from Anoxic Freshwater Sediment. *Int. J. Syst. Bacteriol.* 1997, 47, 754.

(75) King, E., Brodie, E. L., Anantharaman, K., et al. A new approach to predict microbial community assembly and function using a stochastic, genome-enabled modeling framework. In AGU Fall Meeting, San Francisco, CA, USA, 2015.

(76) Allison, S. D. A trait-based approach for modelling microbial litter decomposition. *Ecology Letters* 2012, 15 (9), 1058–1070.

(77) Bouskill, N. J.; Tang, J.; Riley, W. J.; Brodie, E. L. Trait-based representation of biological nitrification: Model development, testing, and predicted community composition. *Front. Microbiol.* 2012, 3(OCT), DOI: 10.3389/fmicb.2012.00364.

(78) McClain, M. E.; Boyer, E. W.; Dent, C. L.; et al. Biogeochemical Hot Spots and Hot Moments at the Interface of Terrestrial and Aquatic Ecosystems. *Ecosystems* 2003, 6 (4), 301–312.

(79) Salehikhoo, F.; Li, L. The role of magnesite spatial distribution patterns in determining dissolution rates: When do they matter? *Geochim. Cosmochim. Acta* 2015, 155, 107–121.

(80) Perujo, N.; Sanchez-Vila, X.; Proia, L.; Romani, A. M. Interaction between Physical Heterogeneity and Microbial Processes in Subsurface Sediments: A Laboratory-Scale Column Experiment. *Environ. Sci. Technol.* 2017, 51 (11), 6110–6119.